Single-molecule imaging of IQGAP1 regulating actin filament dynamics

Gregory J. Hoeprich, Amy N. Sinclair, Shashank Shekhar†, and Bruce L. Goode*
Department of Biology, Brandeis University, Waltham, MA 02453

ABSTRACT **IQGAP is a conserved family of actin-binding proteins with essential roles in cell motility, cytokinesis, and cell adhesion, yet there remains a limited understanding of how IQGAP proteins directly influence actin filament dynamics. To close this gap, we used single-molecule and single-filament total internal reflection fluorescence microscopy to observe IQGAP regulating actin dynamics in real time. To our knowledge, this is the first study to do so. Our results demonstrate that full-length human IQGAP1 forms dimers that stably bind to actin filament sides and transiently cap barbed ends. These interactions organize filaments into thin bundles, suppress barbed end growth, and inhibit filament disassembly. Surprisingly, each activity depends on distinct combinations of IQGAP1 domains and/or dimerization, suggesting that different mechanisms underlie each functional effect on actin. These observations have important implications for how IQGAP functions as an actin regulator in vivo and how it may be regulated in different biological settings.**

Monitoring Editor
Laurent Blanchoin
CEA Grenoble

Received: Apr 27, 2021
Revised: Oct 6, 2021
Accepted: Oct 25, 2021

INTRODUCTION

IQGAP is a large multidomain actin-binding protein that is conserved across the animal and fungal kingdoms (Shannon, 2012) and plays crucial roles in cytokinesis, cell migration, phagocytosis, and cell adhesion (Kuroda *et al.*, 1996; Epp and Chant, 1997; Mataraza *et al.*, 2003; Wu *et al.*, 2003). The founding member of this protein family, human IQGAP1, was identified in 1994 and named based on its sequence similarity to GTPase-activating protein (GAP) proteins (Weissbach *et al.*, 1994). Subsequently, IQGAP1 was shown to interact with Cdc42 and Rac1 but was found to lack GAP activity. Instead, IQGAP1 stabilizes Cdc42 in its active GTP-bound form (Hart *et al.*, 1996; Kuroda *et al.*, 1996). Mammals have three IQGAP genes (IQGAP1–3), with IQGAP1 being the best characterized (Hedman *et al.*, 2015). IQGAP1 functions directly downstream of Cdc42 and Rac1 at the leading edge and is required for polarized cell migration and proper lamellipodial protrusion dynamics (Hart *et al.*, 1996; Kuroda *et al.*, 1996). Up-regulated IQGAP1 expression promotes motility (Mataraza *et al.*, 2003) and is associated with aggressive cancers and tumorigenesis (Dong *et al.*, 2006; Jadeski *et al.*, 2008; White *et al.*, 2009).

IQGAP1 is often referred to and/or depicted as a "scaffold" protein because it associates with a number of different cytoskeletal regulatory proteins, including N-WASP, adenomatous polyposis coli (APC), CLIP-170, CLASP, and the formin Dia1 (Figure 1A) (Fukata *et al.*, 2002; Watanabe *et al.*, 2004; Brandt *et al.*, 2007; Le Clainche *et al.*, 2007). However, IQGAP1 also directly binds to actin filaments (Bashour *et al.*, 1997; Fukata *et al.*, 1997; Pelikan-Conchaudron *et al.*, 2011). Thus, a key step in understanding how IQGAP1 functions in vivo is to precisely define the kinetics of its associations with actin filaments and its direct regulatory effects on actin filament dynamics. To date, only a single study has investigated the in vitro effects of an IQGAP protein on actin filament dynamics, in which bulk pyrene-actin assembly assays were used to show that IQGAP1 slows barbed end growth and stabilizes filaments (Pelikan-Conchaudron *et al.*, 2011). This has left many open questions about IQGAP's activities and mechanism, which can be difficult to answer using bulk assays due to their inherent limitations. While bulk assays have been

---

Competing interests: The authors declare no competing financial interests.

†Present address: Departments of Physics and Cell Biology, Emory University, Atlanta, GA 30322.

Author contributions: G.J.H. and B.L.G. designed the experiments and wrote the manuscript. G.J.H., S.S., and A.N.S. performed experiments. G.J.H. and S.S. analyzed the data.

*Address correspondence to: Bruce L. Goode (goode@brandeis.edu).

Abbreviations used: BSA, bovine serum albumin; DTT, dithiothreitol; EGTA, ethylene glycol-bis(β-aminoethyl ether)-*N*,*N*,*N*′,*N*′-tetraacetic acid; FWHM, full-width half-max; GAP, GTPase activating protein; GTP, guanosine triphosphate; IPTG, isopropyl β-D-1-thiogalactopyranoside; IQGAP1, IQ-domain GTPase-activating protein 1; K_d, equilibrium dissociation constant; mf-TIRF, microfluidic total internal reflection fluorescence; OG, Oregon Green; PMSF, phenylmethylsulfonyl fluoride; RMA, rabbit skeletal muscle actin; SD, standard deviation; SEM, standard error of the mean; TIRF, total internal reflection fluorescence.

used extensively to quantify the effects of actin-binding proteins, they are sometimes not as effective as direct observation in distinguishing between effects on filament nucleation versus elongation, or between effects from severing versus depolymerization in filament disassembly assays. Further, bulk assays report on the collective behavior of the entire filament population, averaged, and thus are unable to resolve two or more simultaneous, distinct effects on actin. For instance, the VCA domain of WAVE1 enhances Arp2/3 complex-dependent actin nucleation activity but also reduces the barbed end elongation rate (independently of its interactions with Arp2/3 complex), and these two effects offset each other in bulk assays but are readily distinguishable in total internal reflection fluorescence (TIRF) assays (Sweeney *et al.*, 2015).

Here, we have overcome these limitations by using TIRF microscopy to observe the effects of human IQGAP1 on the dynamics of individual actin filaments and to monitor single molecules of IQGAP1 interacting with filaments in real time (Smith *et al.*, 2014; Shekhar and Carlier, 2016). Our results show that full-length IQGAP1 forms dimers that tightly associate with filament sides and 1) transiently cap barbed ends to pause filament growth, 2) organize filaments into thin bundles, and 3) stabilize filaments against depolymerization. Further, we assign roles for the N- and C-terminal actin-binding halves of IQGAP1 in these activities and provide additional evidence for distinct mechanisms underlying each regulatory effect on actin. Overall, our results confirm the major conclusions from previous bulk studies but also provide a number of new mechanistic insights into how IQGAP family proteins directly influence actin filament dynamics and spatial organization, with important implications for IQGAP in vivo functions and regulation.

RESULTS

IQGAP1 transiently caps barbed ends of actin filaments

We initiated our investigation by directly observing the effects of purified human IQGAP1 on actin filament barbed end growth using conventional open-flow TIRF assays. Oregon green (OG)-labeled actin filaments were polymerized in open-flow TIRF chambers and sparsely tethered by incorporation of a low percentage of biotin-actin subunits (Figure 1B). Monitoring polymerization allowed us to identify the fast-growing barbed ends and measure their rate of growth. In control reactions, barbed ends grew at 7.4 ± 1.8 subunits s^{-1} μM^{-1} (Figure 1C), consistent with previous studies (Breitsprecher *et al.*, 2012; Alioto *et al.*, 2016). The addition of nanomolar concentrations of full-length IQGAP1 led to fewer and shorter filaments in the fields of view (FOVs) (Figure 1B and Supplemental Video 1), exhibiting a concentration-dependent reduction in barbed end growth rate (Figure 1C). These effects were potent, as 80 nM IQGAP1 was sufficient to strongly inhibit elongation (1.0 ± 0.7 subunit s^{-1} μM^{-1}). We attribute the reduced number of actin filaments per FOV to the inhibitory effects of IQGAP1 on elongation because it offers the simplest explanation. Alternatively, IQGAP1 could suppress spontaneous actin nucleation, but this seems less likely given that there is no evidence for IQGAP1 binding G-actin.

To better understand the mechanism of barbed end inhibition, we generated traces of filament length over time, focusing on reactions containing 20 nM IQGAP1, which exhibited an intermediate level of inhibition (Figure 1D and Supplemental Figure S1A). Our reasoning was that these reactions would give us the best chance of detecting potential pauses in growth (capping events). This analysis revealed alternating phases of growth and no growth at filament barbed ends, suggesting that IQGAP1 transiently blocks barbed end growth rather than persistently slowing growth. Consistent with this hypothesis, the barbed end growth rate that occurred between pauses was the same as the growth rate throughout control reactions lacking IQGAP1 (Supplemental Figure S1B). Direct observation of filaments in real time was essential to uncovering the transient capping activity.

To determine the off rate of IQGAP1 from barbed ends, we measured the durations of the pauses in growth induced by IQGAP1 (example blue traces, Figure 1D). Control reactions showed much shorter interruptions (86.3% were ≤10 s; average 5.1 s), which are due to the inherent noise in the assay (see *Materials and Methods*) (example control traces in gray, Figure 1D). Therefore, we excluded interruptions of ≤10 s in our analysis of pauses induced by IQGAP1. This analysis yielded an off rate of 0.039 s^{-1}, corresponding to an average pause time of ~26 s (Figure 1E). As expected, at a lower concentration of IQGAP1 (1.4 nM) the average pause time was similar (~21 s; off rate 0.048 s^{-1}) (Supplemental Figure S1C) while the frequency of pausing was greatly reduced (Supplemental Figure S1D). We could not measure the on rate from these data because the elongation times between pauses were not differentiable from control (Supplemental Figure S1E). Instead, we determined the on rate by first calculating the affinity (K_d) of IQGAP1's interaction with barbed ends, which was achieved by plotting the fraction of free growing ends versus IQGAP1 concentration, K_d = 25 nM (inset, Figure 1C). Then, using the experimentally determined K_d and off rate, we calculated the on rate, which was 1.56×10^6 s^{-1} M^{-1} (Figure 1E).

To determine whether the concentrations of IQGAP1 required to inhibit barbed end growth in vitro are physiologically relevant, we used quantitative Western blotting to define the concentration of IQGAP1 in U2OS osteosarcoma cells (Figure 1F). The average from three experiments was 405 nM ± 112 (mean and SD), which is well above the in vitro concentrations that strongly inhibited barbed end growth in our TIRF experiments. These values were also similar to the reported IQGAP1 concentration in MTD-1A epithelial cells (~300 nM) (Fukata *et al.*, 1997). Importantly, F-actin levels in mammalian cell lines are estimated to be >200 µM (Pollard *et al.*, 2000; Koestler *et al.*, 2009), suggesting that only a small percentage of the F-actin in cells could possibly be decorated by IQGAP1. This idea is also consistent with the specificity of IQGAP1 localization to actin networks at the leading edge (Hart *et al.*, 1996; Kuroda *et al.*, 1996; Bashour *et al.*, 1997). Further, the concentration of IQGAP1 is sufficiently high in cells to efficiently cap barbed ends where it localizes, and we suggest that this capping activity may help promote the assembly of actin networks by suppressing their disassembly (see the *Discussion*).

Full-length IQGAP1 and its N-terminal half tightly bind to actin filament sides

To define the kinetics of IQGAP1 interactions with actin filaments, we purified and fluorescently labeled SNAP-tagged full-length IQGAP1 (649-SNAP-IQGAP1). Importantly, the addition of the tag and the dye did not alter IQGAP1 suppression of barbed end growth (Supplemental Figure S2A). We first analyzed the oligomeric state of our protein. Previous structural studies have suggested the presence of a strong dimerization activity in the W-IQ region (763–863) and a weaker dimerization activity in the N-terminus adjacent to the calponin homology (CH) domain (Fukata *et al.*, 1997; Ren *et al.*, 2005; LeCour *et al.*, 2016; Liu *et al.*, 2016). The presence of multiple dimerization domains in IQGAP1 has left it unclear whether the full-length protein exists in higher-order oligomerization states beyond dimers. On the other hand, equilibrium sedimentation analysis has suggested that full-length IQGAP1 forms dimers (Bashour *et al.*, 1997). Therefore, as an independent test of the oligomerization state, we performed step-photobleaching analysis on labeled

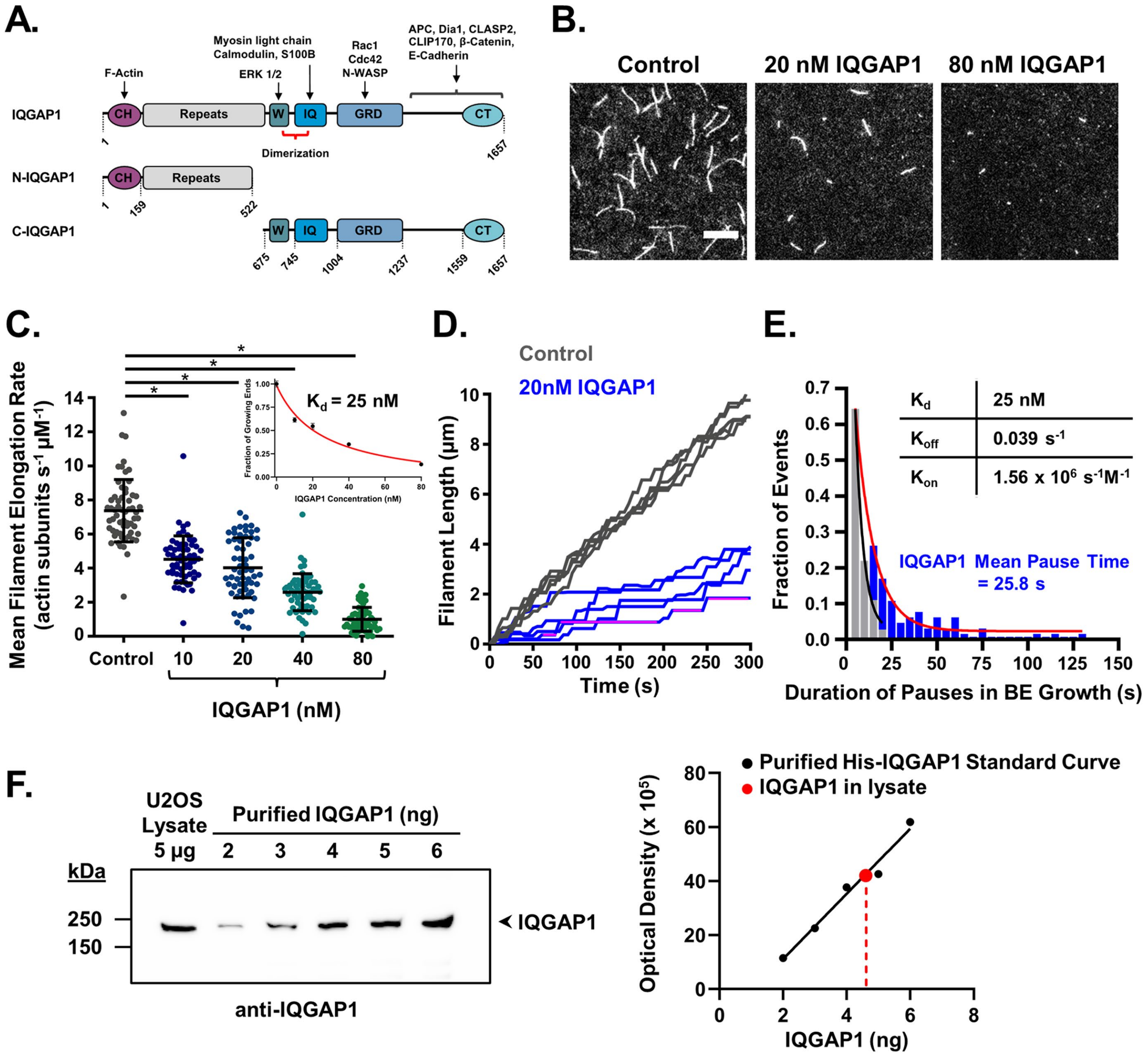

FIGURE 1: IQGAP1 transiently caps actin filament ends to inhibit barbed end growth. (A) Domain layouts for full-length IQGAP1 and fragments used in this study. Domains: CH, calponin homology; Repeats, six 50-amino-acid repeats; W, WW domain; IQ, four isoleucine–glutamine motifs; GRD, GAP-related domain; CT, C-terminal domain. Amino acid numbering and boundaries are from UniProt: P46940, PDB: 1 × 0H and structural work (Abel *et al.*, 2015; LeCour *et al.*, 2016). Binding partners of different domains are shown. (B) Representative images from open-flow TIRF microscopy assays 10 min after initiation of actin assembly. Reactions contain 1 µM G-actin (10% Oregon green–labeled, 0.5% biotin-labeled) and different concentrations of full-length IQGAP1. Scale bar, 10 µm. (C) Barbed end elongation rates for actin filaments in TIRF reactions as in B ($n = 60$ filaments, pooled from three independent trials for each condition). Mean and SD. Student's *t* test was used to determine the statistical significance of differences between conditions (* $p < 0.05$). Inset graph: fraction of free growing barbed ends vs. concentration of IQGAP1 (nM) fitted with a hyperbolic binding curve to measure the equilibrium binding constant ($K_d = 25$ nM). Error bars, SEM. (D) Example traces of individual filament lengths over time (five each) for control reactions and reactions containing 20 nM IQGAP1, from the same reactions as in C. Note the increase in pause time (no growth) in the presence of 20 nM IQGAP1 (example pauses for one filament trace highlighted by magenta lines). (E) Duration of pauses in the presence of 20 nM IQGAP1 (blue histogram, red curve, $n =$ 10 filaments, and 65 pause events) compared with control (gray histogram, black curve, $n = 10$ filaments, and 176 pause events). The mean barbed end pause time in the control reactions (lacking IQGAP1) was 5.1 s and in the presence of 20 nM IQGAP1 was 25.8 s. Fits were calculated from a single exponential equation. Inset: table listing IQGAP1 binding affinity, on rate, and off rate for the barbed end. (F) Representative quantitative Western blot (one of three independent trials) used to determine the concentration of endogenous IQGAP1 in U2OS cells. Blot was probed with anti-IQGAP1 antibody to compare the signal for endogenous IQGAP1 in the cell lysate lane to known quantities of purified 6His-IQGAP1. A standard curve was generated from the signals on the blot. The average cellular concentration of IQGAP1 (405 nM ± 112) was calculated from values obtained in three independent trials (482, 276, and 458 nM).

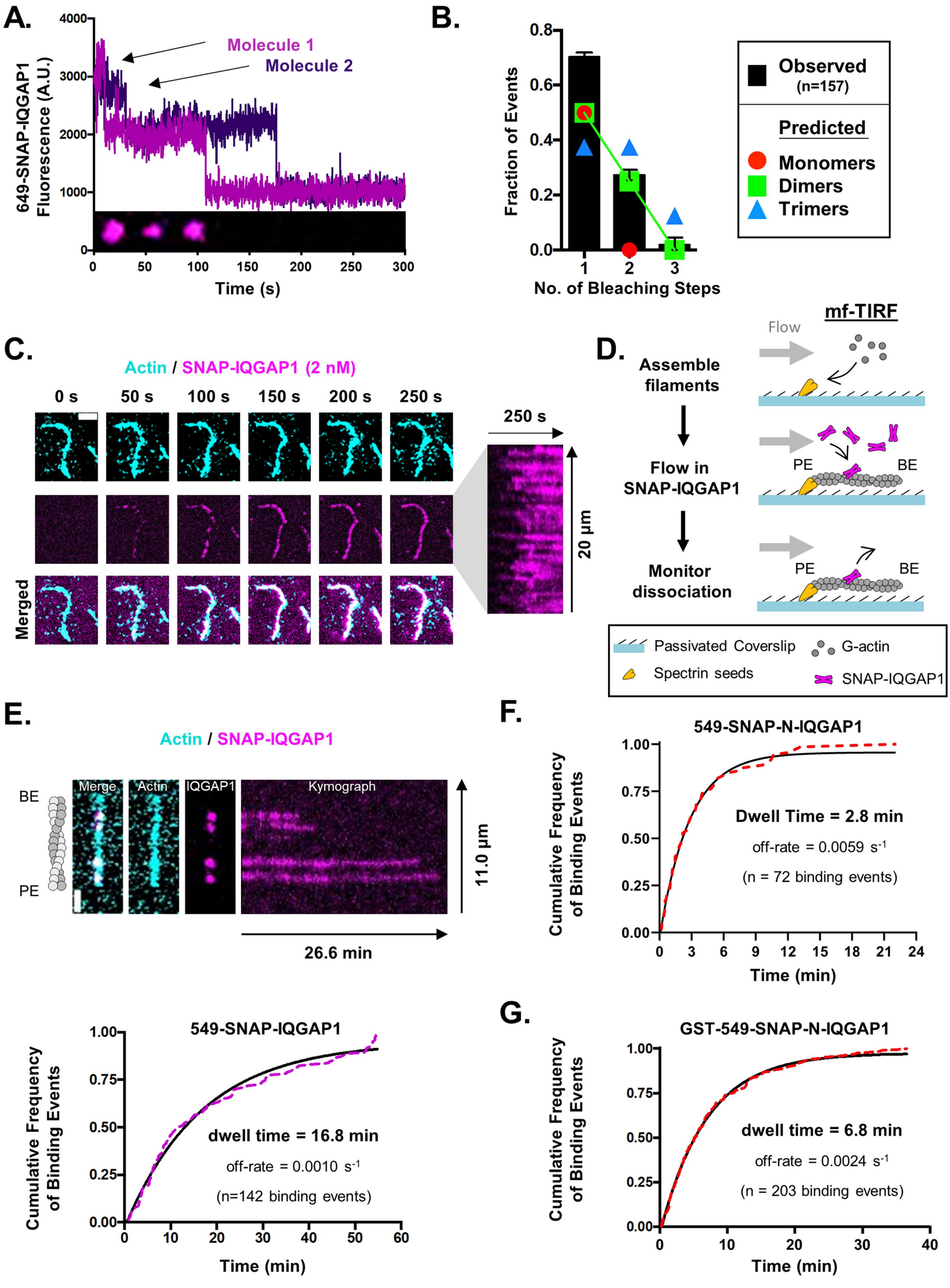
A.
649-SNAP-IQGAP1 Fluorescence (A.U.)
4000
3000
2000
1000
0
Molecule 1
Molecule 2
0
50
100
150
200
250
300
Time (s)
B.
Fraction of Events
0.8
0.6
0.4
0.2
0.0
1
2
3
No. of Bleaching Steps
Observed (n=157)
Predicted
Monomers
Dimers
Trimers
C.
Actin / SNAP-IQGAP1 (2 nM)
0 s
50 s
100 s
150 s
200 s
250 s
Merged
250 s
20 µm
D.
mf-TIRF
Flow
Assemble filaments
Flow in SNAP-IQGAP1
Monitor dissociation
PE
BE
Passivated Coverslip
G-actin
Spectrin seeds
SNAP-IQGAP1
E.
Actin / SNAP-IQGAP1
BE
PE
Merge
Actin
IQGAP1
Kymograph
11.0 µm
26.6 min
549-SNAP-IQGAP1
Cumulative Frequency of Binding Events
1.00
0.75
0.50
0.25
0.00
0
10
20
30
40
50
60
Time (min)
dwell time = 16.8 min
off-rate = 0.0010 s-1
(n=142 binding events)
F.
549-SNAP-N-IQGAP1
Cumulative Frequency of Binding Events
1.00
0.75
0.50
0.25
0.00
0
3
6
9
12
15
18
21
24
Time (min)
Dwell Time = 2.8 min
off-rate = 0.0059 s-1
(n = 72 binding events)
G.
GST-549-SNAP-N-IQGAP1
Cumulative Frequency of Binding Events
1.00
0.75
0.50
0.25
0.00
0
10
20
30
40
Time (min)
dwell time = 6.8 min
off-rate = 0.0024 s-1
(n = 203 binding events)

full-length IQGAP1 molecules. Our results show that full-length IQGAP1 (with or without an N-terminal GST-tag) forms stable dimers (Figure 2, A and B, and Supplemental Figure S2B, left panel), with little evidence of higher-order oligomerization, agreeing with the above sedimentation study. Further, labeled full-length IQGAP1 had the same oligomerization state (dimeric) when bound to actin filament sides (Supplemental Figure S2B, right panel).

We attempted to monitor 649-SNAP-IQGAP1 molecules interacting with filament sides using open-flow TIRF microscopy, where filaments were first assembled and tethered and then a low concentration (2 nM) of 649-SNAP-IQGAP1 was flowed in. Under these conditions, we could readily detect binding of 649-SNAP-IQGAP1 molecules to filament sides early in the reactions. However, binding was very stable, which meant that filaments steadily accumulated IQGAP1 on their sides, making it difficult to detect dissociation events (Figure 2C). For this reason, we turned to using microfluidics-assisted TIRF (mf-TIRF), which allows new ingredients to be flowed in and out of the chambers and aligns and straightens filaments under flow, providing more accurate measurements of filament length (Jegou *et al*., 2011a,b; Shekhar, 2017). In these assays, we anchored filaments at their pointed ends to grow them by barbed end polymerization. We next briefly flowed in 649-SNAP-IQGAP1 (without actin monomers) to allow binding and then washed free molecules out in order to monitor dissociation events in the absence of new binding events (Figure 2D). The average lifetime of 649-SNAP-IQGAP1 binding on filament sides was 16.8 min, corresponding to an off rate of 0.001 s^{-1} (Figure 2E). To control for photobleaching effects, we repeated the analysis at a reduced frequency of image capture and obtained an off rate that was not statistically different (Supplemental Figure S2C). Thus, full-length IQGAP1 interacts with filament sides very stably, consistent with a high-affinity interaction.

In addition, we attempted to analyze 649-SNAP-IQGAP1 interactions with the barbed ends of filaments. However, this was extremely challenging due to the much stronger side-binding affinity compared with end-binding affinity. Moreover, at low concentrations of labeled IQGAP1 when we observed a single-molecule binding near the barbed end, the limited resolution of light microscopy precluded us from knowing whether the molecule was capping the barbed end or instead binding one of the ~80 side-binding sites located within 200 nm of the barbed end.

To better understand which domains in IQGAP1 are responsible for its dimerization and interactions with actin filament sides, we purified and labeled a SNAP-tagged N-terminal fragment of IQGAP1 (1–522), with and without a GST tag (Figure 1A). On the basis of previous studies, we expected that the non–GST-tagged N-IQGAP1 polypeptide would be monomeric because it lacks the dimerizing W-IQ region (Ren *et al.*, 2005) (Supplemental Figure S3A), which we confirmed by step-photobleaching analysis (Supplemental Figure S3B). Further, the GST-tagged 549-SNAP-N-IQGAP1 polypeptide was dimeric (Supplemental Figure S3C). Similar results were obtained for nontagged and GST-tagged SNAP-N-IQGAP1 molecules bound to filament sides (Supplemental Figure S3, D and E).

Using mf-TIRF assays as above for full-length IQGAP1, we found that monomeric 549-SNAP-N-IQGAP1 molecules stably interacted with filament sides with an average dwell time of 2.8 min, corresponding to an off rate of 0.006 s^{-1} (Figure 2F). Dimeric GST-tagged 549-SNAP-N-IQGAP1 molecules had an average dwell time of 6.8 min, corresponding to an off rate of 0.0025 s^{-1} (Figure 2G). Together, our data show that the monomeric N-terminal half of IQGAP1 (1–522) is sufficient to stably bind actin filament sides and suggest that the C-terminal half of IQGAP1 makes only a modest contribution to filament side binding.

We also purified a SNAP-tagged C-terminal fragment of IQGAP1 (675–1657), 649-SNAP-C-IQGAP1, in an attempt to analyze its association with filaments. However, it did not bind to filament sides (Supplemental Figure S4A), and it failed to suppress barbed end growth (Supplemental Figure S4B), suggesting that the SNAP tag may interfere with actin binding. Moreover, we swapped the position of the SNAP tag to the C-terminal end of the polypeptide, but this fusion protein was insoluble.

Inhibition of barbed end growth by the N- and C-terminal halves of IQGAP1

Next, we asked whether the inhibitory effects of IQGAP1 on barbed end growth are mediated by its N- and/or C-terminal halves. Using

FIGURE 2: IQGAP1 dimers bind stably to the sides of actin filaments. (A) Representative step photobleaching traces from single molecules of full-length 649-SNAP-IQGAP1. Plot shows fluorescence intensity over time. Inset shows montage of images for one of the molecules shown in the plot (molecule 1, magenta). (B) Fraction of 649-SNAP-IQGAP1 molecules (*n* = 157) that photobleached in one, two, or three steps (>3 photobleaching steps was never observed) from analysis as in A. Error bars, SEM. Observed fraction of photobleaching events (black) is compared with the predicted fraction of photobleaching events (based on SNAP-labeling efficiency [Breitsprecher *et al*., 2012]) for different oligomeric states (color-coded symbols). (C) Representative time-lapse images and kymograph from TIRF reaction containing 2 nM 649-SNAP-IQGAP1, showing molecules (magenta) binding to an actin filament (cyan). Scale bar, 2 µm. Kymograph shows that 649-SNAP-IQGAP1 decoration is distributed along the filament over time. (D) Schematic showing experimental strategy to monitor 649-SNAP-IQGAP1 dissociation from filaments by mf-TIRF. Actin filaments with free barbed ends were polymerized from coverslip-anchored spectrin-actin seeds in the presence of 1 µM G-actin (15% Alexa-488-labeled) and 5 µM profilin and then capped at their barbed ends by flowing in 100 nM mouse capping protein (CP) for 1 min to prevent subsequent disassembly. Next, 0.5 nM 649-SNAP-IQGAP1 (without actin) was flowed in for 1 min to allow binding to filament sides, then buffer was flowed in (to remove free 649-SNAP-IQGAP1), and dissociation of 649-SNAP-IQGAP1 molecules was monitored over time. PE, pointed end; BE, barbed end.
(E) Representative image and kymograph of 649-SNAP-IQGAP1 molecules (magenta) bound to an actin filament (cyan). Scale bar, 2 µm. Observed dwell times (*n* = 142 binding events) were plotted (dotted line), and an exponential fit (black line) was used to calculate the average dwell time of 16.8 min. (F) Observed dwell times of 549-SNAP-N-IQGAP1 molecules (*n* = 72 binding events) were plotted (dotted line), and an exponential fit (black line) was used to calculate the average dwell time of 2.8 min. (G) Observed dwell times of GST-549-SNAP-N-IQGAP1 molecules (*n* = 203 binding events) were plotted (dotted line), and an exponential fit (black line) was used to calculate the average dwell time of 6.8 min.

open-flow TIRF microscopy, we compared the activities of different concentrations of N-IQGAP1 and C-IQGAP1 (Figure 3). Increasing concentrations of either fragment resulted in fewer and shorter filaments (Figure 3A), and each fragment alone caused a concentration-dependent decrease in barbed end growth rate (Figure 3, B and C). Interestingly, the inhibitory effects of each fragment alone plateaued at ~50% of the control rate of growth, whereas full-length IQGAP1 almost completely suppressed growth (Figure 3D). Furthermore, adding both halves (N-IQGAP1 and C-IQGAP1) *in trans* failed to improve the inhibitory effects beyond those of each fragment alone (Figure 3C; also see arrow in Figure 3D), suggesting that full inhibition requires both halves to be physically linked. It is unclear why neither half of IQGAP1 alone completely inhibits barbed end growth, but it is possible that each half alone only partially obstructs monomer addition at barbed ends. It is also interesting that the two halves of the protein *in trans* do not reconstitute the full inhibitory effects of the intact protein, which future structural studies may help resolve.

Similar to full-length IQGAP1, N-IQGAP1 and C-IQGAP1 fragments induced pauses in barbed end growth (example traces in Supplemental Figure S5). Average pause times and off rates were analyzed as above for full-length IQGAP1: N-IQGAP1 (18.4 s, 0.055 s^{-1} off rate) and C-IQGAP1 (14.7 s, 0.068 s^{-1} off rate) (Figure 3E). To estimate the on rates of each fragment (for binding the barbed end), we calculated their equilibrium constants (K_d) by plotting the fraction of free growing ends versus N-IQGAP1 and C-IQGAP1 concentrations (N-IQGAP1 K_d ~17 nM; C-IQGAP K_d ~24 nM). Using the experimentally determined affinities (K_d) and off rates, we estimated the on rates for N-IQGAP1 (3.2×10^6 s^{-1} M^{-1}) and C-IQGAP1 (2.8×10^6 s^{-1} M^{-1}).

Finally, while our C-IQGAP1$^{675-1657}$ construct only partially suppressed actin assembly in TIRF assays, a shorter construct,

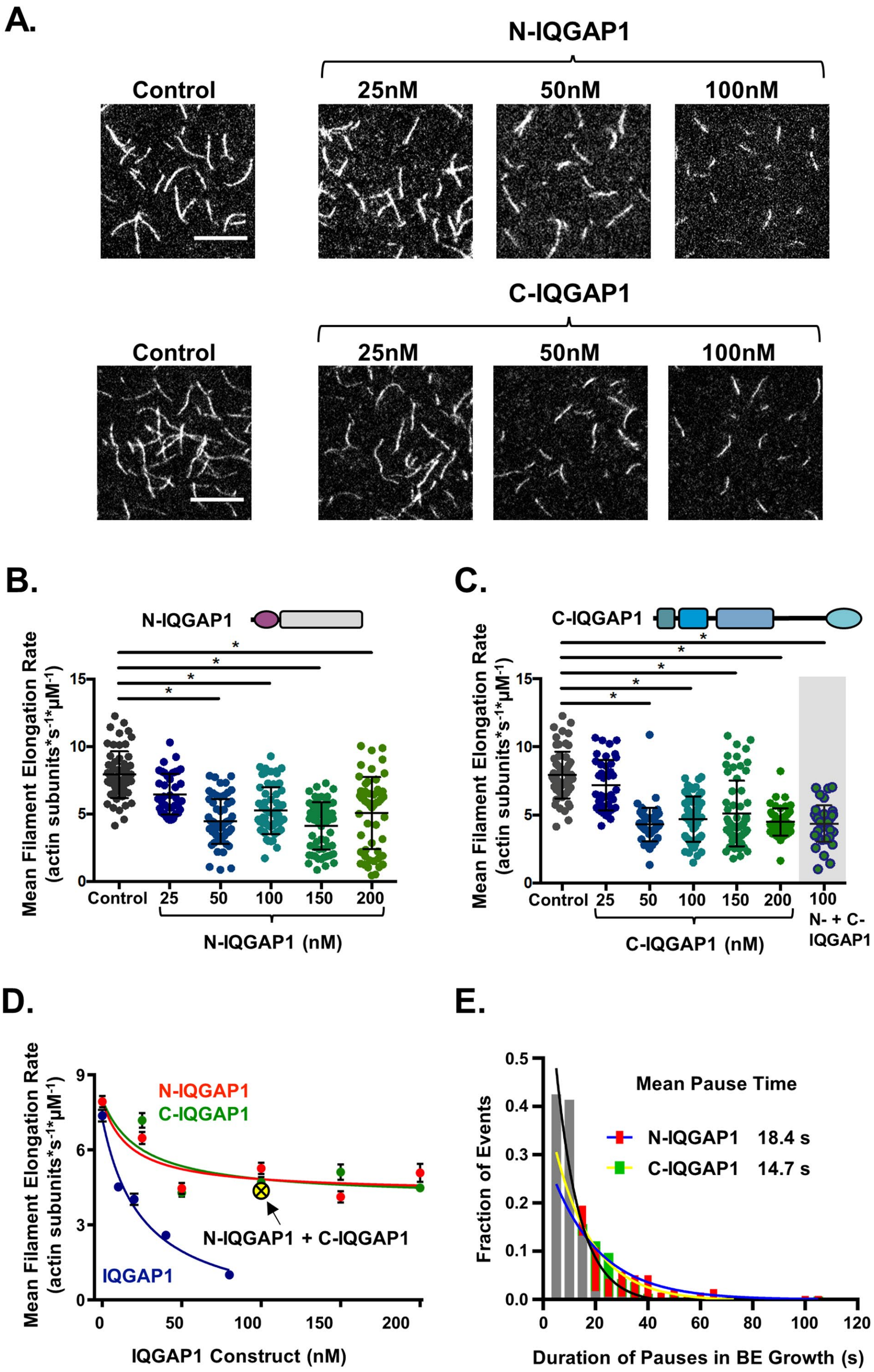

FIGURE 3: Each half of IQGAP1 partially suppresses actin filament growth. (A) Representative images from open-flow TIRF microscopy assays 10 min after initiation of actin assembly. Reactions contain 1 µM G-actin (10% Oregon green–labeled, 0.5% biotin-labeled) and different concentrations of N-IQGAP1 or C-IQGAP1. Scale bar, 10 µm. (B) Barbed end growth rates for filaments in TIRF reactions as in A, comparing the effects of different concentrations of N-IQGAP1. Data pooled from three independent trials (number of filaments analyzed for each condition, left to right: 60, 40, 60, 60, 60, and 55). Mean and SD. Student's *t* test was used to determine the statistical significance of differences between conditions (* $p < 0.05$). (C) Same as B, except for the testing variable concentrations of C-IQGAP1 (number of filaments analyzed for each condition, left to right: 60, 40, 60, 60, 60, 55, and 40). Gray shaded data show the combined effects of N-IQGAP1 and C-IQGAP1 (100 nM each) on barbed end elongation rate. (D) Comparison of concentration-dependent effects of full-length IQGAP1 (data from Figure 1C), N-IQGAP1 (data from B), and C-IQGAP1 (data from C) on barbed end growth rate. For each, the data were fitted to a single exponential decay curve. Error bars, SEM. Yellow dot highlights the combined effects of N-IQGAP1 and C-IQGAP1 (100 nM each). (E) Duration of pauses in barbed end growth for 50 nM N-IQGAP1 (red histogram, blue curve, $n = 10$ filaments and 139 pause events) and 50 nM C-IQGAP1 (green histogram, yellow curve, $n = 10$ filaments and 166 pause events) compared with control reactions (gray histogram, black curve, $n = 10$ filaments and 174 pause events). Fits were calculated from a single exponential equation.

C-IQGAP1$^{744–1657}$, was previously reported to more fully inhibit actin assembly in bulk assays (Pelikan-Conchaudron *et al.*, 2011). This apparent discrepancy prompted us to purify and directly compare the effects of C-IQGAP1$^{675–1657}$ and C-IQGAP1$^{744–1657}$ (GST tags removed) in both bulk assays and open-flow TIRF assays (Supplemental Figure S6). In the study of Pelikan-Conchaudron *et al.* (2011), 330 nM C-IQGAP1$^{744–1657}$ was sufficient to completely inhibit barbed end assembly. However, we found that even higher concentrations (400 and 500 nM) of C-IQGAP1$^{675–1657}$ and C-IQGAP1$^{744–1657}$ only partially suppressed assembly in both assays. These data are also consistent with our observations using GST-tagged C-IQGAP1$^{675–1657}$, where the capping effects leveled off at ~50% (Figure 3D). Thus, all of our data from three different constructs in two different assays support the view that the C-terminal half of IQGAP1 only partially blocks barbed end growth.

Dimerization of the N-terminal half of IQGAP1 promotes actin filament bundling

Using open-flow TIRF microscopy, we examined how IQGAP1 affects the spatial organization of actin filaments. 649-SNAP-IQGAP1 was flowed into TIRF chambers containing preassembled (nonanchored) actin filaments (5–10 µm long), and over time the filament sides became increasingly decorated by IQGAP1 and grew thicker, that is, formed bundles (Figure 4A and Supplemental Video 2). To understand which domain(s) of IQGAP1 mediate bundling, we compared the effects of 10 nM full-length IQGAP1, N-IQGAP1, and C-IQGAP1 on preassembled (nonanchored) filaments (Figure 4B). N-IQGAP1 induced weak bundling compared with full-length IQGAP1, and C-IQGAP1 lacked significant bundling activity (Figure 4, B and C). The thickness of the bundles was assessed by two methods: 1) measuring fluorescence intensity along the length of the bundles and calculating fluorescence density per micron of bundle length (Figure 4C); 2) measuring fluorescence intensity of a fixed-width line segment drawn perpendicular to the bundle (Figure 4D). By both methods, full-length IQGAP1 approximately tripled the fluorescence/thickness of filaments, suggesting formation of bundles approximately three filaments thick. In contrast, N-IQGAP1 increased the fluorescence/thickness of filaments only ~1.5-fold, indicating a reduced bundling activity compared with full-length IQGAP1. Thus, bundling effects are substantially reduced by loss of the C-terminal half of IQGAP1. We considered whether the C-terminus, which contains the dimerization domain, is important for bundling because it dimerizes the N-terminus. To test this idea, we compared the bundling activities of 10 nM monomeric N-IQGAP1 and GST-dimerized N-IQGAP1 (Figure 4E). GST-tagged N-IQGAP1 organized filaments into bundles of thickness similar to those organized by full-length IQGAP1. These data suggest that dimerization is required for efficient bundling and that while the N-terminal half provides the F-actin side binding, the C-terminal half of IQGAP1 provides dimerization.

The monomeric N-terminal half of IQGAP1 stabilizes filaments against depolymerization

IQGAP1 suppresses dilution-induced F-actin disassembly in bulk assays (Pelikan-Conchaudron *et al.*, 2011). Given that filaments depolymerize more rapidly from their barbed ends than from their pointed ends in the absence of actin monomers (Pollard, 1986), we used mf-TIRF assays to monitor the effects of IQGAP1 on barbed end depolymerization of individual filaments in real time. Filaments anchored at their pointed ends were first polymerized, and then different concentrations of full-length IQGAP1 (without actin monomers) were flowed in and depolymerization at the barbed end was monitored (Figure 5, A and B, and Supplemental Video 3). At 1 nM IQGAP1, the depolymerization rate was reduced by ~90% (0.6 subunit s^{-1} ± 0.9, vs. 6.0 subunits s^{-1} ± 2.9 in control reactions), and in the presence of 10 nM IQGAP1 depolymerization was almost undetectable (0.1 subunit s^{-1} ± 0.1) (Figure 5B). The concentration of full-length IQGAP1 required for half-maximal change in depolymerization rate (IC_{50}) was only 0.1 nM (Figure 5C).

Additional analysis by mf-TIRF revealed that N-IQGAP1 potently stabilizes filaments against depolymerization at their barbed ends, nearly as well as full-length IQGAP1 (Figure 5, B and C). In contrast, C-IQGAP1 was >100-fold less potent than full-length IQGAP1 in stabilizing filaments. These observations suggest that monomeric N-IQGAP1 plays the dominant role in stabilizing filaments. This observation was somewhat unexpected, given the importance of C-IQGAP1 in inhibiting filament growth at barbed ends, and suggests that these two regulatory effects (inhibition of barbed end growth and stabilization of filaments against depolymerization) have distinct underlying mechanisms.

To provide additional insights into how IQGAP1 stabilizes filaments, we performed single-molecule mf-TIRF experiments in which we monitored barbed end depolymerization on filaments sparsely decorated with single molecules of 649-SNAP-IQGAP1. We observed that depolymerization proceeded at the control rate until it reached a 649-SNAP-IQGAP1 molecule on the filament side, where it abruptly halted for minutes (Figure 5D). Depolymerization never proceeded while the 649-SNAP-IQGAP1 molecule was bound to the filament side (18 out of 18 events). These observations indicate that a single molecule of IQGAP1 on the side of a filament is sufficient to halt depolymerization. To our knowledge, such effects have not been described for any other actin filament side-binding protein. Given the potency of these stabilization effects, combined with the very slow dissociation rate of IQGAP1 from filament sides, even sparse decoration by IQGAP1 in vivo may be sufficient to dramatically suppress the dynamics of cellular actin networks.

DISCUSSION

In a wide range of organisms IQGAP family proteins perform critical roles in controlling cellular actin dynamics, and yet there have been few in vitro studies to date investigating the nature of IQGAP's direct regulatory influence on actin filament dynamics. Our analysis using TIRF microscopy helps close this gap by providing the first direct visualization of an IQGAP family protein interacting with actin filaments and regulating their dynamics and spatial organization in real time. Below we discuss each of our key observations and their relevance to understanding IQGAP's in vivo roles as an actin regulator.

Kinetics of IQGAP1 interactions with actin filaments

Previous studies using cosedimentation assays hinted that IQGAP1 binds to actin filaments with high affinity but did not quantify the interaction (Bashour *et al.*, 1997). Using single-molecule analysis, we have directly observed and quantified the interactions of full-length human IQGAP1 molecules with the sides of filaments (dwell time ~17 min; off rate 0.001 s^{-1}). Given that full-length IQGAP1 dimerizes, we considered the possibility that its high affinity binding might stem from having two separate CH domains, because dissociation of IQGAP1 would then require simultaneous unbinding of both CH domains. However, we discovered that monomeric N-IQGAP1 is sufficient to bind filament sides with relatively high affinity (dwell time ~2.8 min; off rate 0.006 s^{-1}). Thus, our results suggest that a single CH domain (possibly with contributions from flanking sequences) is sufficient to mediate a stable association with filament sides.

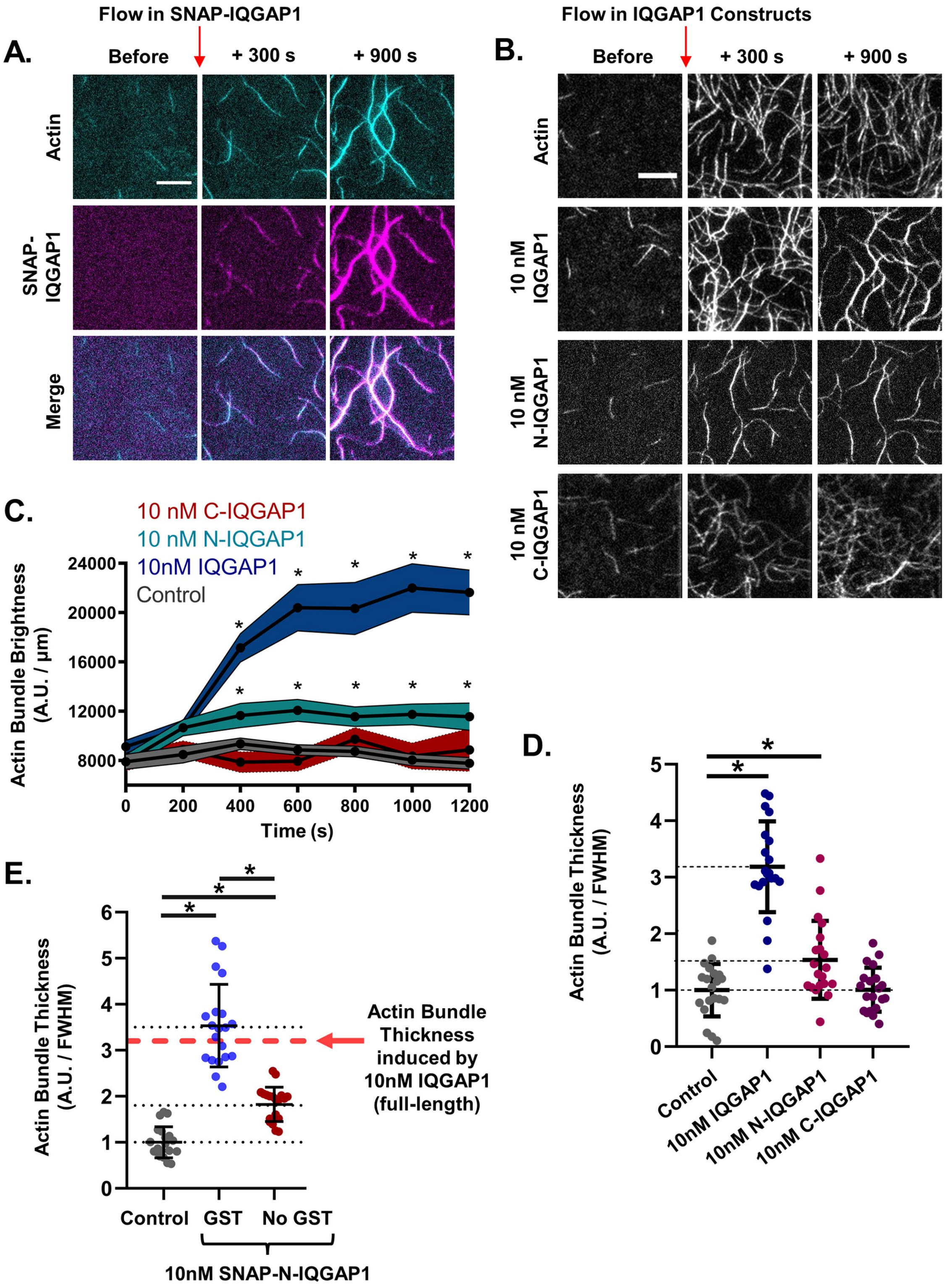

FIGURE 4: Dimerization of N-IQGAP1 promotes actin filament bundling. (A) Representative time-lapse images from open-flow TIRF microscopy reactions containing 2 µM F-actin (10% Oregon green–labeled) and 2 nM 649-SNAP-IQGAP1. Scale bar, 10 µm. (B) Representative time-lapse images from TIRF microscopy reactions containing 2 µM F-actin (10% Oregon green–labeled) grown to 5–10 µm and then 10 nM IQGAP1, N-IQGAP1, or C-IQGAP1 was flowed into the reaction chamber. Scale bar, 10 µm. IQGAP1 (or control buffer) was flowed in 300 s after initiation of actin assembly, when filaments had grown to lengths of 5–10 µm. (C) Change in bundle thickness over time for reactions as in B, determined by measuring the fluorescence intensity along a bundle and calculating the fluorescence density per unit length. Student's *t* test was used to determine the statistical significance of the increase in fluorescence observed after time zero (* $p < 0.05$). (D) Bundle thickness was also assessed by measuring fluorescence intensity at FWHM of line segments drawn perpendicular to the bundle. The fluorescence intensity values were normalized to control (2 µM

One in vivo implication of IQGAP family proteins having such a high affinity for actin filaments is that they may competitively block the binding of other CH domain family proteins, for example, fimbrin, filamin, calponin/transgelin, α-actinin, and MICAL (Korenbaum and Rivero, 2002). Indeed, the cytokinetic actin ring (CAR) in fission yeast is heavily decorated by IQGAP (also called Rng2) and less so by α-actinin and fimbrin (Wu and Pollard, 2005). The CH domain is also crucial for the essential function of *Saccharomyces cerevisiae* IQGAP in cytokinesis (Shannon and Li, 1999), consistent with its importance in binding to actin filaments. The high-affinity actin-binding interactions of IQGAP proteins further suggests that this association may require tight regulation in vivo, for example, posttranslational modifications on IQGAP1 that reduce its actin-binding affinity (Grohmanova *et al.*, 2004) and/or allosteric inhibition by ligands such as calmodulin (Ho *et al.*, 1999; Mateer *et al.*, 2002).

Inhibition of barbed end growth

Using TIRF microscopy, we directly observed IQGAP1 inhibiting barbed end elongation. Further, by analyzing the change in filament length over time, we determined that IQGAP1 transiently caps barbed ends (dwell time ~26 s; off rate 0.039 s^{-1}; K_d = 25 nM). For comparison, conventional capping protein associates with barbed ends for tens of minutes (Wear *et al.*, 2003; Johnston *et al.*, 2018). Thus, IQGAP1 appears to be a transient capper.

Earlier bulk studies concluded that IQGAP1's inhibitory effects on filament growth are mediated by the C-terminal half of the protein (Pelikan-Conchaudron *et al.*, 2011). However, we found that full inhibition of elongation requires both halves of IQGAP1. Whereas full-length IQGAP1 almost completely blocked barbed end growth, either half alone (N-IQGAP1 and C-IQGAP1) led to only ~50% inhibition. Thus, our analysis reveals an important role for the N-terminal half in facilitating inhibition of barbed end growth. We considered whether the C-terminal half, which contains the dimerization domain (763–863) (Ren *et al.*, 2005), enhances capping simply by dimerizing the otherwise monomeric N-IQGAP1. However, C-IQGAP1 alone was sufficient to inhibit barbed end growth equally well as N-IQGAP1. Thus, N-IQGAP1 and C-IQGAP1 make separate and complementary contributions to the inhibition of barbed end growth. Future structural studies are required to determine the precise underlying mechanisms. However, it is possible that binding of the CH domain of N-IQGAP1 to filament sides slows the addition of new subunits via allosteric effects, consistent with a study showing that binding of the N-terminus of *Schizosaccharomyces pom*be IQGAP (Rng2) alters the structure of the actin filament (Hayakawa *et al.*, 2020). Although the actin-binding domain of C-IQGAP1 is not as well characterized as the CH domain, this half of the protein is required for full inhibition, and our data suggest that it must be physically linked to N-IQGAP1 to do so (Figure 3D). This suggests that close coordination between the two actin-binding domains of IQGAP1 is required for full inhibition (see model, Figure 6).

How might transient barbed end capping by IQGAP1 contribute to its in vivo functions? IQGAP1 accumulates at the leading edge of cells and is required for normal lamellipodia protrusion velocity and frequency (Hart *et al.*, 1996; Kuroda *et al.*, 1996; Bashour *et al.*, 1997; Mataraza *et al.*, 2003). Furthermore, IQGAP1 is thought to promote actin assembly at the leading edge through interactions with N-WASP (Bensenor *et al.*, 2007; Le Clainche *et al.*, 2007) and Dia1 (Brandt *et al.*, 2007). How would transient capping help promote actin network assembly? Although capping suppresses the growth of individual actin filaments in a purified system, in a cellular context capping is not synonymous with "negative regulation." This is because capping in vivo focuses actin monomer addition to the newly nucleated barbed ends via a "funneling" effect (Loisel *et al.*, 1999; Shekhar and Carlier, 2017) and elevates actin monomer concentrations to help promote nucleation (Akin and Mullins, 2008). Thus, under cellular conditions capping can play an important role in promoting actin network assembly.

Actin filament bundling

Earlier studies using electron microscopy and falling ball viscosity assays demonstrated that IQGAP1 cross-links actin filaments and that this activity is mediated by N-terminal CH domain–containing fragments of the protein (1–216) (Fukata *et al.*, 1997). Fukata *et al.* (1997) found that the minimal construct (1–863) that cross-links filaments included both the CH domain and the suggested dimerization domain (763–863) Ren *et al.* (2005). In TIRF assays, we found that IQGAP1 potently bundles actin filaments (10 nM was sufficient to bundle 2 µM F-actin). Further, we measured bundle thickness and found that full-length IQGAP1 organizes filaments into thin bundles, only a few filaments thick. In agreement with Fukata *et al.* (1997). we observed that bundling requires dimerization of the N-terminal half of IQGAP1, by either a GST tag or inclusion of the C-terminal half, which contains the dimerization domain (see model, Figure 6). Bundling by IQGAP1 may be important for its role in promoting cell motility, cell adhesion, and cytokinesis. Further, bundling by IQGAP1 may be regulated in vivo, and indeed calmodulin binding inhibits IQGAP1's bundling effects (Mateer *et al.*, 2002). In addition, Cdc42 and Rac1 binding to the GRD region of IQGAP1 may lead to its higher-order oligomerization (Fukata *et al.*, 1997), potentially expanding or transforming its filament cross-linking capabilities.

Stabilization of actin filaments

We found that IQGAP1 potently stabilizes actin filaments against depolymerization in TIRF assays (Figure 5B). Interestingly, monomeric N-IQGAP1 and dimeric full-length IQGAP1 had similar half-maximal inhibitory concentrations (IC_{50}s) (0.1 and 0.3 nM, respectively). These results validate earlier observations from bulk assays (Pelikan-Conchaudron *et al.*, 2011) and extend our understanding of the mechanism by showing that the monomeric N-terminal half is sufficient for these effects. In addition, our results show that IQGAP1 stabilizes filaments independent of bundling. Many CH domain–containing proteins cross-link filaments as well as stabilizing them against depolymerization, for example, calponin, fimbrin, and IQGAP1 (Goodman *et al.*, 2003; Pelikan-Conchaudron *et al.*, 2011). This has suggested that the cross-linking and stabilization activities of CH domain family proteins may be coupled. However, we directly tested this model by monitoring IQGAP1 stabilization of single (nonbundled) actin filaments in mf-TIRF assays. In this manner, we uncoupled stabilization from bundling, which is not possible to do using bulk assays. It is interesting to note that while monomeric

---

F-actin). Student's *t* test was used to determine the statistical significance of differences between conditions (* $p < 0.05$).
(E) Comparing monomeric vs dimeric N-IQGAP1 fragments bundling actin filaments by measuring fluorescence intensity at FWHM of a line segment drawn perpendicular to the bundle. The fluorescence intensity values were normalized to control (2 µM F-actin). Student's *t* test was used to determine the statistical significance of differences between conditions (* $p < 0.05$).

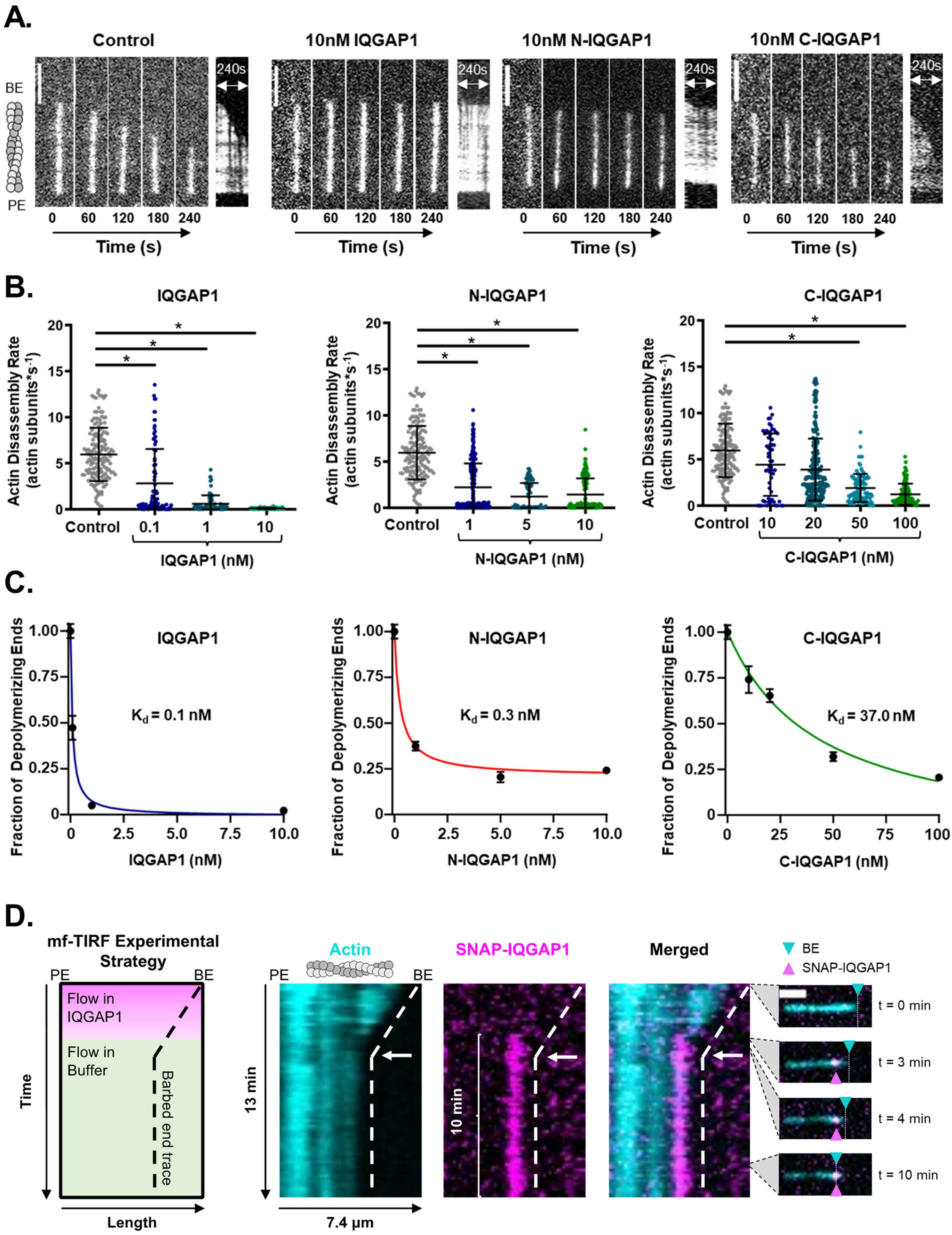
A.
Control
10nM IQGAP1
10nM N-IQGAP1
10nM C-IQGAP1
BE
PE
240s
0 60 120 180 240
Time (s)
B.
IQGAP1
N-IQGAP1
C-IQGAP1
Actin Disassembly Rate (actin subunits*s-1)
*
Control 0.1 1 10
IQGAP1 (nM)
Control 1 5 10
N-IQGAP1 (nM)
Control 10 20 50 100
C-IQGAP1 (nM)
C.
Fraction of Depolymerizing Ends
IQGAP1
Kd = 0.1 nM
IQGAP1 (nM)
N-IQGAP1
Kd = 0.3 nM
N-IQGAP1 (nM)
C-IQGAP1
Kd = 37.0 nM
C-IQGAP1 (nM)
D.
mf-TIRF Experimental Strategy
PE
BE
Flow in IQGAP1
Flow in Buffer
Barbed end trace
Time
Length
Actin
SNAP-IQGAP1
Merged
13 min
10 min
7.4 µm
BE
SNAP-IQGAP1
t = 0 min
t = 3 min
t = 4 min
t = 10 min

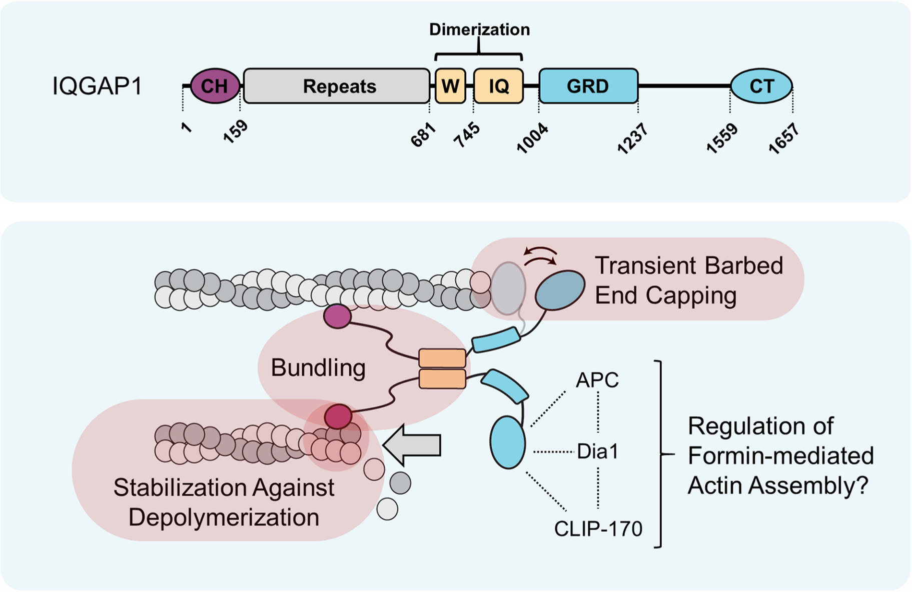

FIGURE 6: Working model for IQGAP1 regulatory activities on actin filament dynamics and spatial organization. Top panel shows domain layout of full-length IQGAP1. Bottom panel shows working model for how IQGAP1 dimers directly control actin filament growth, bundling, and stabilization, with each activity highlighted in red. The N-terminal half of IQGAP1 binds tightly to filament sides using its CH domain and plays a central role in stabilizing filaments. Dimerization of the N-terminal half is mediated by the W-IQ region of IQGAP1, which is required for bundling but not stabilization. C-terminal domains in IQGAP1 transiently cap the barbed end, attenuating filament elongation. Importantly, the C-terminal domains work in close coordination with the N-terminal side-binding half of IQGAP1 to achieve full inhibition of elongation. The C-terminal (CT) domain of IQGAP1 binds to the formin Dia1, as well as CLIP-170 and adenomatous polyposis coli (APC), which directly collaborate with Dia1 to promote actin assembly (Fukata *et al.*, 2002; Watanabe *et al.*, 2004; Brandt *et al.*, 2007; Lewkowicz *et al.*, 2008; Okada *et al.*, 2010; Breitsprecher *et al.*, 2012; Henty-Ridilla *et al.*, 2016). Thus, IQGAP1 may have additional regulatory roles in controlling formin- and APC-mediated actin assembly, but it is not clear how these suggested roles of the C-terminal half are coordinated with its transient capping effects on the barbed end.

N-IQGAP1 is sufficient to potently stabilize filaments, it has minimal bundling activity (Figure 4E). Taken together, these observations suggest that stabilization can occur independently of bundling and that while the CH domain appears to be required for both stabilization and bundling, bundling additionally requires dimerization (Figure 6). This has important implications for IQGAP1 functions in vivo, as it suggests that IQGAP1's bundling effects could be regulated independently of its stabilization effects on actin networks.

Concluding remarks

In this study, we have used direct observation by TIRF microscopy to 1) define the kinetics of IQGAP1 single-molecule interactions with actin filament sides and barbed ends, 2) define IQGAP1's regulatory effects on actin filament dynamics and spatial organization, and 3) determine the contributions of each half of IQGAP1 to these activities. Our results show that IQGAP1 is a high-affinity actin-binding protein that potently stabilizes filaments against depolymerization and suppresses barbed end elongation. As discussed above, these activities help to explain the in vivo roles of IQGAP family proteins in promoting actin assembly to facilitate such processes as cell migration, cell adhesion, and cytokinesis. Interestingly, another recent study found that IQGAP proteins tethered to lipid membranes generate highly curved actin filament structures, for example, arcs and rings (Palani *et al.*, 2021). Together with our study, this provides an important mechanistic framework for future investigations aimed at understanding how IQGAP works with in vivo binding partners (e.g., calmodulin, Cdc42, Dia1, APC, and CLIP-170) to govern actin dynamics at the leading edge (Hart *et al.*, 1996; Bashour *et al.*, 1997; Grohmanova *et al.*, 2004; Roy *et al.*, 2004; Watanabe *et al.*, 2004; Brandt *et al.*, 2007; Le Clainche *et al.*, 2007). Several of these ligands bind to a C-terminal domain in IQGAP1, suggesting

---

FIGURE 5: The monomeric N-terminal half of IQGAP1 strongly suppresses depolymerization at barbed ends. (A) Representative time-lapse images and kymographs of fluorescently labeled actin filaments (10% Oregon green–labeled actin) in mf-TIRF reactions, comparing depolymerization from barbed ends in the presence of 10 nM IQGAP1, N-IQGAP1, C-IQGAP1, or control buffer. Filaments anchored at their pointed ends were polymerized, and then IQGAP1, N-IQGAP1, or C-IQGAP1 (without actin monomers) was flowed in at time zero and depolymerization was monitored over time. Scale bar, 5 μm. (B) Barbed end depolymerization rates measured in the presence of different concentrations of IQGAP1, N-IQGAP1, and C-IQGAP1. Data pooled from three independent trials (number of filaments analyzed for each condition, left to right: 160, 93, 75, 68, 160, 315, 74, 221, 160, 59, 249, 107, and 103). Mean and SD. Student's *t* test was used to determine the statistical significance of differences between conditions (* $p < 0.05$). (C) Graphs showing fraction of free depolymerizing barbed ends vs. concentration of IQGAP1, N-IQGAP1, or C-IQGAP1, in which a hyperbolic binding curve was fitted to the data to determine the equilibrium binding constant (K_d). Error bars, SEM. Note that N-IQGAP1 is nearly as potent as full-length IQGAP1 in suppressing depolymerization, whereas C-IQGAP1 is ~300-fold weaker. (D) mf-TIRF experiment (and representative kymograph) showing arrest of barbed end depolymerization where a 649-SNAP-IQGAP1 molecule is bound to the side of a filament. Left panel shows experimental scheme. Actin filaments with free barbed ends were first polymerized from coverslip-anchored spectrin-actin seeds in the presence of 1 μM G-actin (15% Alexa-488–labeled) and 5 μM profilin. Next, 0.4 nM 649-SNAP-IQGAP1 (without actin) was flowed in for 4 min to allow binding to filament sides, then buffer alone was flowed in, and depolymerization was monitored. PE, pointed end; BE, barbed end. The example kymograph shows depolymerization halting (white arrow) where the 649-SNAP-IQGAP1 molecule is bound to the filament side. Select time points from the merged kymograph (t = 0, 3, 4, 10 min) highlight barbed end depolymerization (cyan arrowhead) halting at 649-SNAP-IQGAP1 molecule (magenta arrowhead). Scale bar = 2 μm.

that their activities may be coordinated with the transient capping activity of IQGAP1 to control actin assembly (Figure 6).

MATERIALS AND METHODS

Request a protocol through *Bio-protocol*.

Plasmid construction

Plasmids for *Escherichia coli* expression and purification of human full-length 6His-IQGAP1 (1–1657), 6His-N-IQGAP1 (1–522), and GST-C-IQGAP1 (675–1657) were generously provided by Marie-France Carlier (CNRS, Paris). The resulting tagged proteins are referred to as IQGAP1, N-IQGAP1, and C-IQGAP1 throughout this study; the GST tag (on C-IQGAP1) was removed only where specifically indicated. To generate plasmids for *E. coli* expression and purification of the same three IQGAP1 polypeptides with SNAP tags, coding regions from the above plasmids were PCR amplified and subcloned into the GST-pp-SNAP-pGEX-6p-1 vector (Breitsprecher *et al.*, 2012), which introduces an N-terminal GST tag, PreScission Protease site (pp), and SNAP tag, and a C-terminal 6His tag. SNAP-IQGAP1 proteins used in this study include all of these tags, except where it is noted that the GST tag was removed.

Protein purification

Rabbit skeletal muscle actin (RMA) was purified from acetone powder (Spudich and Watt, 1971) generated from frozen ground hind leg muscle tissue of young rabbits (Pel-Freez Biologicals, Rogers, AR). Lyophilized acetone powder stored at –80°C was mechanically sheared in a coffee grinder, resuspended in G-buffer (5 mM Tris-HCl, pH 8.0, 0.2 mM ATP, 0.5 mM dithiothreitol [DTT], 0.1 mM $CaCl_2$), and then cleared by centrifugation for 20 min at 50,000 × *g*, 4°C). The supernatant was filtered through Grade 1 Whatman paper and then the actin was polymerized by the addition of 2 mM $MgCl_2$ and 50 mM NaCl to the filtrate and overnight incubation at 4°C with slow stirring. The next morning, NaCl powder was added to a final 0.6 M, and stirring was continued for another 30 min at 4°C. F-actin was pelleted by centrifugation for 150 min at 120,000 × *g*, 4°C. The pellet was solubilized by dounce homogenization and dialyzed against 1 l of G-buffer at 4°C (three consecutive times at 12–18 h intervals). Monomeric actin was then precleared for 30 min at 435,000 × *g*, 4°C, and loaded onto a S200 (16/60) gel-filtration column (GE Healthcare; Marlborough, MA). Peak fractions containing actin were stored at 4°C.

For preparing biotinylated actin used in open-flow cell TIRF microscopy assays, the F-actin pellet above was dounce homogenized and dialyzed against G-buffer lacking DTT. Monomeric actin was then polymerized by the addition of an equal volume of 2× labeling buffer (50 mM imidazole, pH 7.5, 200 mM KCl, 0.3 mM ATP, and 4 mM $MgCl_2$). After 5 min, the actin was mixed with a fivefold molar excess of NHS-XX-Biotin (Merck KGaA, Darmstadt, Germany) and incubated for 15 h at 4°C. The F-actin was pelleted as above, and the pellet was rinsed with G-buffer, then homogenized with a dounce, and dialyzed against G-buffer for 48 h at 4°C. Biotinylated monomeric actin was purified further on an S200 (16/60) gel-filtration column as above. Aliquots of biotin actin were snap frozen in liquid N_2 and stored at –80°C.

For the fluorescently labeled actin used in open-flow cell TIRF microscopy assays, actin was labeled on cysteine 374 as previously described (Kuhn and Pollard, 2005). Briefly, the F-actin pellet described above was dounce homogenized and dialyzed against G-buffer lacking DTT. Monomeric actin was then polymerized by adding an equal volume of 2× labeling buffer (50 mM imidazole pH 7.5, 200 mM KCl, 0.3 mM ATP, 4 mM $MgCl_2$). After 5 min, the actin was mixed with a fivefold molar excess of Oregon green (OG)-488 iodoacetamide (Life Technologies, Carlsbad, CA), resuspended in anhydrous dimethylformamide, and incubated in the dark for 15 h at 4°C. Labeled F-actin was pelleted as above, and the pellet was rinsed briefly with G-buffer, then depolymerized by dounce homogenization, and dialyzed against G-buffer for 2 d at 4°C. Labeled, monomeric actin was purified further on a 16/60 S200 gel-filtration column as above. OG-488-actin was dialyzed for 15 h against G-buffer with 50% glycerol and stored at –20°C. The concentration and labeling efficiency were determined by measuring the absorbance at 280 and 496 nm, using these molar extinction coefficients: ε_{280} actin = 45,840 M^{-1} cm^{-1}, ε_{496} OG-488 = 76,000 M^{-1} cm^{-1}, and OG-488 correction factor at 280 = 0.12.

For the fluorescently labeled actin used in mf-TIRF assays, actin was labeled on surface-exposed primary amines as previously described (Shekhar, 2017). Briefly, G-actin was polymerized by dialyzing overnight against modified F-buffer (20 mM PIPES, pH 6.9, 0.2 mM $CaCl_2$, 0.2 mM ATP, 100 mM KCl). Then the F-actin was incubated for 2 h at room temperature with a fivefold molar excess of Alexa-488 NHS ester dye (Life Technologies). F-actin was then pelleted by centrifugation at 450,000 × *g* for 40 min at room temperature. The pellet was resuspended in G-buffer, homogenized with a dounce, and incubated on ice for 2 h to depolymerize filaments. Actin was then repolymerized on ice for 1 h after adding KCl and $MgCl_2$ (final concentrations of 100 and 1 mM, respectively). F-actin was pelleted by centrifugation for 40 min at 450,000 × *g* at 4°C. The pellet was homogenized with a dounce and dialyzed overnight at 4°C against 1 l of G-buffer. Next, the solution was centrifuged for 40 min at 450,000 × *g* at 4°C, and the supernatant was collected. The concentration and labeling efficiency were determined by measuring the absorbance at 280 and 495 nm, using these molar extinction coefficients: ε_{280} actin = 45,840 M^{-1} cm^{-1}, ε_{495} Alexa-488 = 71,000 M^{-1} cm^{-1}, and ε_{280} AF488 = 7810 M^{-1} cm^{-1}.

Human profilin-1 was expressed in *E. coli* BL21 DE3 by growing cells to log phase at 37°C in Terrific Broth (TB) media and inducing expression with 1 mM isopropyl β-D-1-thiogalactopyranoside PMSF: phenylmethylsulfonyl fluoride (IPTG) at 37°C for 3 h. Cells were harvested by centrifugation, and pellets were stored at –80°C. Cell pellets were resuspended in lysis buffer (50 mM Tris-HCl, pH 8.0, 1 mM EDTA, 0.2% Triton X-100, lysozyme, 1 mM PMSF, and protease inhibitor cocktail: 0.5 μM each of pepstatin A, antipain, leupeptin, aprotinin, and chymostatin) and kept on ice for 30 min. Lysates were cleared for 30 min at 272,000 × *g* at 4°C, and the supernatant was collected and fractionated on a HiTrap Q column (GE Healthcare, Chicago, IL) equilibrated in 20 mM Tris, pH 8.0, and 50 mM NaCl and eluted with a salt gradient (0–1 M NaCl and 20 mM Tris, pH 8.0). Peak fractions were concentrated and then purified further on a Superdex 75 column equilibrated in 20 mM Tris-HCl, pH 8.0, and 50 mM NaCl. Peak fractions were pooled, snap frozen in aliquots, and stored at –80°C.

Mouse nonmuscle capping protein (CPa1b2 or CP) was purified as described (Graziano *et al.*, 2014). Briefly, the expression vector (Soeno *et al.*, 1998) was expressed in *E. coli* BL21 pLysS by growing cells to log phase at 37°C in Lauryl Broth media and inducing expression with 0.4 mM IPTG at 37°C for 3 h. Cells were harvested by centrifugation, and pellets were stored at –80°C. Cell pellets were resuspended in lysis buffer (20 mM Tris, pH 8.0, 1 mM EDTA, 0.1% Triton X-100, lysozyme, a standard mixture of protease inhibitors) and kept on ice for 30 min. Lysates were cleared for 30 min at 12,500 × *g* at 4°C, and the supernatant was collected and fractionated on a 1 ml Q-HiTrap column (GE Healthcare) equilibrated in 20 mM Tris, pH 8.0, and 50 mM NaCl and eluted with a salt gradient (0–0.5 M

NaCl and 20 mM Tris, pH 8.0). Peak fractions were concentrated and then purified further on a Superdex 75 gel filtration column (GE Healthcare) equilibrated in 50 mM KCl, 20 mM Tris, pH 8.0. Peak fractions were pooled, dialyzed overnight at 4°C into HEK buffer (20 mM HEPES, pH 7.4, 1 mM EDTA, 50 mM KCl), aliquoted, snap frozen in liquid N_2, and stored at –80°C.

IQGAP1 polypeptides (6His-IQGAP1, 6His-N-IQGAP1, GST-C-IQGAP1) were expressed in *E. coli* BL21(DE3) pRARE by growing cells to log phase in TB and inducing expression with 1 mM IPTG overnight at 16°C. Cells were harvested by centrifugation and pellets stored at –80°C. Cell pellets were resuspended in lysis buffer (50 mM potassium phosphate, pH 8.0, 50 mM imidazole, 500 mM KCl, 1 mM EDTA, pH 8.0, 1 mM DTT, 1% Triton X-100, 20 µg/ml DNase, lysozyme, 1 mM PMSF, and a standard mixture of protease inhibitors), kept on ice for 30 min to allow digestion, and then sonicated. Lysates were cleared for 30 min at 65,000 × *g*. For 6His-IQGAP1 and 6His-N-IQGAP1, precleared lysates were mixed with 1 ml Ni-NTA-agarose beads (Qiagen, Hilden, Germany) and incubated for 1 h rotating at 4°C. Beads were then washed three times with Ni-NTA wash buffer (20 mM Tris, pH 8.0, 50 mM imidazole, 500 mM KCl, and 0.3% glycerol). Proteins were eluted in Ni-NTA elution buffer (Ni-NTA wash buffer plus for 500 mM imidazole). For GST-C-IQGAP1, the precleared lysate was mixed with 1 ml of glutathione-agarose beads (Thermo Fisher Scientific, Waltham, MA) and incubated for 1 h rotating at 4°C. Beads were then washed three times with GST wash buffer (20 mM Tris, pH 8.0, 500 mM KCl, and 5% glycerol) and eluted in GST elution buffer (GST wash buffer supplemented with 20 mM Reduced Glutathione [Sigma; St. Louis, MO]). All eluates were concentrated, cleared by low-speed centrifugation, and gel filtered on a Superose 12 10/300 GL column (GE Healthcare) equilibrated in $HEKG_5$ buffer (20 mM HEPES, pH 7.4, 1 mM EDTA, 50 mM KCl, and 5% glycerol). Peak fractions were pooled, concentrated, snap frozen, and stored at –80°C.

SNAP-tagged IQGAP1 polypeptides (GST-SNAP-IQGAP1-6His, GST-SNAP-N-IQGAP1-6His, and GST-SNAP-C-IQGAP1-6His) were purified as above for C-IQGAP1 and fluorescently labeled while still bound to the glutathione-agarose beads. For labeling, 5 µM SNAP-surface549 or SNAP-surface649 (New England Biolabs, Ipswich, MA) was incubated with the beads rotating overnight at 4°C. The next day, the beads were washed with five column volumes of GST wash buffer to remove excess dye, and then proteins were eluted with GST elution buffer. Eluates were concentrated, cleared by low-speed centrifugation, and gel filtered on a Superose 12 10/300 GL column (GE Healthcare) equilibrated in $HEKG_5$ buffer. Peak fractions were pooled, concentrated, snap frozen, and stored at –80°C. For the photobleaching experiments in Supplemental Figure S2B, to control for possible GST effects on the oligomerization state of full-length IQGAP1, the GST tag was removed from 549-SNAP-IQGAP1 by digestion with PreScission Protease during the above labeling step. The percent labeling of polypeptides with SNAP–surface 549 was determined by measuring fluorophore absorbance at ε560, using the extinction coefficient 140,300 M^{-1} cm^{-1}. The percent labeling with SNAP–surface 649 was determined by absorbance at ε655, using the extinction coefficient 250,000 M^{-1} cm^{-1}. Labeling efficiencies were consistently 55%–60%.

Spectrin-actin seeds, for mf-TIRF, were purified from blood as described in Casella *et al.* (1986) and Shekhar (2017). Briefly, packed human red blood cells (20 ml) (Novaseek Research, Cambridge, MA) were washed three times with 25 ml of ice-cold buffer A (5 mM sodium phosphate, pH 7.7, 150 mM NaCl, and 1 mM EDTA), each time centrifuging for 15 min at 2000 × *g* at 4°C, and discarding the supernatant. To lyse cells, the cell pellet was resuspended in 700 ml (approximately 10 times the volume of washed cells) of ice-cold lysis buffer (5 mM sodium phosphate, pH 7.7, and 1 mM PMSF) and incubated for 40 min while stirring at 4°C. The lysate was centrifuged for 15 min at 45,000 × *g* at 4°C. The cloudy and viscous pellets were resuspended in wash buffer B (5 mM sodium phosphate, pH 7.7, and 0.1 mM PMSF), final volume 360 ml, and homogenized by pipetting. Next, the mixture was centrifuged for 15 min at 45,000 × *g* at 4°C. The pellets were resuspended in a total volume of 180 ml of wash buffer B, homogenized as above, and then centrifuged as above. This process was repeated once more. Pellets are translucent at this stage. Next, the spectrin-actin was extracted by resuspending each pellet in 5 ml of extraction buffer (0.3 mM sodium phosphate, pH 7.6, and 0.1 mM PMSF), combining the contents into one tube, adjusting the volume to 60 ml with the same buffer, and centrifuging for 30 min at 60,000 × *g* at 4°C, repeated once. The final pellet was resuspended in an equal volume of extraction buffer and gently vortexed and then incubated for 40 min in a water bath at 37°C while manually inverting the tubes every ~10 min. Finally, the sample was precleared for 30 min at 450,000 × *g* at 4°C. DTT (2 mM final) and protease inhibitors were added to the cleared supernatant, and an equal volume of cold glycerol (50% final concentration) was mixed into the solution. Spectrin-actin seeds were aliquoted and stored at –20°C.

Open-flow TIRF microscopy

Glass coverslips (60 × 24 mm; Thermo Fisher Scientific) were first cleaned by sonication in detergent for 60 min, followed by successive sonications in 1 M KOH and 1 M HCl for 20 min each and in ethanol for 60 min. Coverslips were then washed extensively with H_2O and dried in an N_2 stream. The cleaned coverslips were coated with 2 mg/ml methoxy-polyethylene glycol (PEG)-silane MW 2000 and 2 µg/ml biotin-PEG-silane MW 3400 (Laysan Bio, Arab, AL) in 80% ethanol, pH 2.0, and incubated overnight at 70°C. Flow cells were assembled by rinsing PEG-coated coverslips with water, drying with N_2, and adhering to µ-Slide VI0.1 (0.1 × 17 × 1 mm) flow chambers (Ibidi, Fitchburg, WI) with double-sided tape (2.5 cm × 2 mm × 120 µm) and 5-min epoxy resin (Devcon, Danvers, MA). Before each reaction, the flow cell was incubated for 1 min with 4 µg/ml streptavidin in $HEKG_5$ buffer (20 mM HEPES, pH 7.4, 1 mM EDTA, 50 mM KCl, and 5% glycerol), followed by 1 min with 1% bovine serum albumin (BSA) in $HEKG_5$ buffer, and then equilibrated with TIRF buffer (10 mM imidazole, pH 7.4, 50 mM KCl, 1 mM $MgCl_2$, 1 mM ethylene glycol-bis(β-aminoethyl ether)-*N*,*N*,*N*′,*N*′-tetraacetic acid (EGTA), 0.2 mM ATP, 10 mM DTT, 15 mM glucose, 20 µg/ml catalase, 100 µg/ml glucose oxidase) plus 0.5% methylcellulose (4000 cP). Finally, actin and other proteins were flowed in, as specified in the figure captions.

mf-TIRF microscopy

Actin filaments were first assembled in flow cells (Shekhar, 2017). To do this, coverslips were cleaned as above (see *Open-flow TIRF microscopy*) and then coated with an 80% ethanol solution containing 2 mg/ml methoxy-PEG-silane MW 2000 (adjusted to pH 2.0 with HCl) and incubated overnight at 70°C. A 40-µm-high polydimethylsiloxane (PDMS) mold with three inlets and one outlet was mechanically clamped onto a PEG-silane–coated coverslip. The chamber was then connected to a Maesflo microfluidic flow-control system (Fluigent, Chelmsford, MA), rinsed with TIRF buffer, and incubated for 5 min with 1% BSA and 10 µg/ml streptavidin in TIRF buffer. Spectrin-actin seeds in TIRF buffer were passively absorbed to the coverslip for 10 min and then washed with TIRF buffer. Next, 1 µM G-actin (15% Alexa-488 labeled) and 5 µM profilin in TIRF buffer were introduced in order to polymerize actin filaments (with free barbed ends) from the spectrin-actin seeds. Once filaments were polymerized to a desired length (3–10 μm unless otherwise specified), specific proteins were flowed in, as described in the figure captions.

Image acquisition and analysis

Single-wavelength time-lapse TIRF imaging was performed on a Nikon-Ti2000 inverted microscope equipped with a 150-mW argon laser (Melles Griot), a 60× TIRF objective with a numerical aperture of 1.49 (Nikon Instruments), and an electron-multiplying charge-coupled device (EMCCD) camera (Andor Ixon, Belfast, Ireland). One pixel was equivalent to 143 × 143 nm. Focus was maintained by the Perfect Focus system (Nikon Instruments). Open-flow TIRF microscopy images were acquired every 5 s and exposed for 100 ms using imaging software Elements (Nikon Instruments, New York, NY). mf-TIRF microscopy images were exposed every 10 s (or 30 s where noted) and exposed for 100 ms using imaging software Elements (Nikon Instruments).

Images were analyzed in FIJI version 2.0.0-rc-68/1.52e (National Institutes of Health, Bethesda, MD). Background subtraction was conducted using the rolling ball background subtraction algorithm (ball radius, 5 pixels). For open-flow TIRF assays, polymerization rates were determined by plotting the filament length every 25 s and measuring the slope. For mf-TIRF assays, the depolymerization rates were determined by generating kymographs (FIJI kymograph plug-in) from individual filaments. The kymograph slope was used to calculate barbed end depolymerization rates. (Rate measurements assumed one actin subunit contributes 2.7 nm to filament length.) The fraction of growing free barbed ends (not capped by IQGAP1) is plotted in the Figure 1C inset and was calculated by dividing the mean actin filament elongation rate for each condition (IQGAP1 concentration) by the control rate. The resulting binding curves were fitted with the following hyperbolic equation (manually entered into Graphpad Prism 8.0 [San Diego, CA]):

$$P = P_0 + \frac{(P_{\max} - P_0)C}{K + C}$$

where P is the polymerization or depolymerization rate, P_0 is the rate in the absence of IQGAP1 polypeptides, $P_{\max}$ is the rate of polymerization at saturating conditions, K is the IQGAP1 polypeptide concentration at half-saturation, and C is the IQGAP1 polypeptide concentration.

Pauses in barbed end growth were determined from traces of actin filament length versus time (Figure 1D and Supplemental Figure S5). The pause times were plotted in histograms, and distributions were fitted to a one-phase exponential decay equation (Graphpad Prism 8.0) (Figures 1E and 3E and Supplemental Figure S1C). In control reactions (without IQGAP1), the appearance of short interruptions in barbed end growth (average 5.1 s) were due to limited spatiotemporal resolution in the assay, that is, a fast acquisition rate relative to change in filament length over time. At our image acquisition rate (1 frame per 5 s), the mean interruption time (5.1 s) fell within the first two frames acquired. Therefore, we excluded interruptions of ≤10 s from the analysis of what we consider authentic pausing by IQGAP1. We also note that the longest distance across a 143 nm × 143 nm square pixel is ~200 nm (its diagonal). At the control actin elongation rate (1 μM G-actin) of ~8 subunits s^{-1} (or ~22 nm s^{-1}), it takes ~9 s to detect a change in filament length, which further supports exclusion of pauses of ≤10 s from the analysis.

For calculating the dwell times of GST-649-SNAP-IQGAP1, 549-SNAP-IQGAP1 (without GST tag), GST-549-SNAP-N-IQGAP1, and 549-SNAP-N-IQGAP1 molecules on actin filament sides, a kymograph was generated (using the FIJI kymograph plug-in) from individual sparsely decorated filaments. The lifetime measurements of the molecules were plotted, fitted to a one-phase exponential association equation, and used to calculate dwell times (Graphpad Prism 8.0).

For the single-molecule step-photobleaching experiments to determine the oligomerization state, either 2 nM 649-SNAP-IQGAP1 or 2 nM 549-SNAP/Biotin-IQGAP1 in TIRF buffer without glucose oxidase and catalase was transferred into a flow cell as above, and the immobilized spots (either passively absorbed, 649-SNAP-IQGAP1, or anchored by streptavidin-biotin-PEG linkage to the slide surface, 549-SNAP/Biotin-IQGAP1) were subjected to continuous laser exposure with no delay acquisition at 100% laser power. For step-photobleaching experiments in the presence of actin filaments, SNAP-IQGAP1 polypeptides were flowed into an open-flow TIRF chamber with actin filaments already grown to 5–10 μm. Background fluorescence was conducted using the rolling ball background subtraction algorithm (ball radius, 5 pixels). Fluorescence intensities of individual spots were obtained by measuring the mean signal of a 6 × 6 pixel box (~1.5 μm^2) encompassing each spot. Stepwise reductions in the integrated fluorescence intensity time records of individual spots were identified and counted. The oligomeric states of GST-649-SNAP-IQGAP1 (55%–57% labeling efficiency), 549-SNAP-IQGAP1 (without GST tag) (55%–57% labeling efficiency), GST-549-SNAP-N-IQGAP1 (58%–60% labeling efficiency), and 549-SNAP-N-IQGAP1 (58%–60% labeling efficiency) molecules were determined by comparing distributions of the number of photobleaching events to the probability distribution $p(i)$ of the number of fluorescent subunits i predicted for a protein oligomer consisting of n monomers, as calculated from the binomial distribution based on the measured subunit labeling stoichiometry s, as (Breitsprecher *et al.*, 2012)

$$p(i) = \frac{n!}{i!(n-i)!}(s^i(1-s)^{n-i})$$

This approach is expected to be valid because SNAP-tagged protein monomers have only a single site for the benzylguanine-dye adduct.

For actin filament bundling assays, 2 μM monomeric actin (10% Oregon green–labeled) was first polymerized in the TIRF chamber for 5 min at room temperature in TIRF-buffer. After the actin filaments (nonanchored) were grown to 5–10 μm, IQGAP1 polypeptides were flowed in and bundling was monitored for 15 min, acquiring every 5 or 10 s. Upon flowing in IQGAP1, filaments in the TIRF chamber often would move around but did not get flushed out because of the crowding agent (methylcellulose) in the TIRF buffer. Actin filament bundling was measured by subtracting background fluorescence using the rolling ball background subtraction algorithm (ball radius, 50 pixels). The segmented line tool was used to trace all actin filaments/bundles in the FOV. All line segment intensities were then normalized to the length of the measured segment (AU/μm). The intensity measurements were plotted for each time point (every 200 s). Intersections of actin filaments/bundles were excluded from segment measurements as we could not determine whether the intersection was a part of the bundle. To measure the actin bundle thickness, the segmented line tool was used to draw a line perpendicular to actin filaments/bundles in the FOV. The intensity of the line segment was plotted and fitted to a two-dimensional Gaussian in FIJI. The intensity at full-width half-max (FWHM) in for each line trace was measured and recorded 1000 s after flowing in IQGAP1 polypeptides. The thickness of the bundles in the presence of IQGAP1 polypeptides was calculated by normalizing the FWHM intensity to the control reactions.

For mf-TIRF filament disassembly assays, kymographs of individual filaments were generated using the kymograph plug-in in ImageJ. Then the slope from the kymograph was used to calculate the barbed end depolymerization rate of each individual filament (assuming 370 actin subunits per micron). In these experiments, filaments were aged for 10 min (in the absence of actin monomers) before depolymerization was monitored, the kymographs generated show an acceleration of depolymerization at the beginning (Figure 5A). This results from having a mostly ADP-P_i actin at the barbed end (slower depolymerization) and ADP actin (aged actin) farther back from the barbed end (faster polymerization). Therefore, the slopes were measured from the last 2 min of the kymograph.

Quantitative Western blotting

Western blotting was used to determine endogenous IQGAP1 protein levels in U2OS cells (American Type Culture Collection, Manassas, VA). Cells were pelleted and resuspended in lysis buffer (150 mM NaCl, 1.0% NP-40, 1.0% sodium deoxycholate, 1% SDS, 50 mM Tris, pH 7.5, 2 mM EDTA, 0.2 mM sodium orthovanadate, 20 mM β-glycerophosphate, 50 mM sodium fluoride, 1 mM PMSF, 1 mM DTT, and 1× Roche complete protease inhibitor mixture) and incubated at 4°C for 30 min with vortexing every 10 min. Lysates were precleared by centrifugation at 15,300 × *g* for 30 min at 4°C, and the concentration of the soluble protein fraction was determined by Bradford assay (Biorad, Hercules, CA). Known amounts of purified 6His-IQGAP1 were run on gels alongside U2OS cell lysates and blotted with a 1:1000 dilution of rabbit anti-IQGAP1 (ab133490; Abcam, Cambridge, MA). Blots were washed, probed with a 1:10,000 dilution of secondary goat anti-rabbit horseradish peroxidase antibody (Thermo Fisher Scientific), washed again, and then incubated for 1 min with Thermo Scientific SuperSignal West Pico PLUS Chemiluminescent Substrate (Thermo Fisher Scientific). Bands were detected on a BioRad Chemidoc MP imaging system and quantified by densitometry using Imaging Lab version 6.0.1 software (Biorad). A standard curve for the purified protein was generated, and the amount of IQGAP1 protein in the loaded cell lysates was determined by comparison to the standard curve. Values were averaged from three independent blots. For calculations of cellular concentrations of IQGAP1, the concentration of total protein in the cytoplasm was assumed to be 100 mg/ml (Spudich and Watt, 1971). The amount (in grams) of IQGAP1 in 5 µg of lysate was determined, and then the molar concentration of each protein was calculated based on its known molecular weight.

Pyrene-actin assembly assays

Bulk pyrene-actin assays were used to test the effects of purified C-IQGAP1$^{675–1657}$ and C-IQGAP1$^{744–1657}$ polypeptides on actin polymerization. Gel-filtered monomeric actin in G-buffer was cleared by ultracentrifugation for 1 h at 4°C at 350,000 × *g* in a TLA-100 rotor (Beckman Coulter), and the upper ~70% of the supernatant was carefully recovered and used for assembly assays. All reactions (60 µl) contained 2 µM G-actin (5% pyrene labeled), which was converted to Mg^{2+}-ATP-actin 2 min before use. Then, 42 µl of Mg^{2+}-ATP-G-actin was mixed rapidly with 15 µl of proteins or control buffer and 3 µl of 20× initiation mix (40 mM $MgCl_2$, 10 mM ATP, and 1 M KCl) with or without 0.15 mg/ml spectrin-actin seeds to initiate the reactions. Pyrene-actin fluorescence was monitored at an excitation of 365 nm and emission of 407 nm at room temperature for 1500 s in a fluorimeter (Photon Technology International). All assembly traces were normalized to the control curve, which was set to zero.

Data availability

The processed image data for this article have been deposited to Zenodo. In addition, all raw data have been uploaded to a Google Drive and are available upon request to the lead contact (Bruce Goode).

ACKNOWLEDGMENTS

We are grateful to Johnson Chung for assistance with labeling proteins, Jeff Gelles for technical and intellectual input throughout the project, and Colby Fees for valuable comments on the manuscript and assistance with data analysis. We thank Marie-France Carlier for generously providing IQGAP1 plasmids and the Brandeis microfabrication facility for assistance with generating PDMS microfluidic chips for mf-TIRF experiments. This work was supported by a National Institutes of Health R35 award (GM134895) to B.L.G. and the Brandeis NSF MRSEC, Bioinspired Soft Materials, DMR-2011486.

REFERENCES

Abel AM, Schuldt KM, Rajasekaran K, Hwang D, Riese MJ, Rao S, Thakar MS, Malarkannan S (2015). IQGAP1: insights into the function of a molecular puppeteer. Mol Immunol 65, 336–349.

Akin O, Mullins RD (2008). Capping protein increases the rate of actin-based motility by promoting filament nucleation by the Arp2/3 complex. Cell 133, 841–851.

Alioto SL, Garabedian MV, Bellavance DR, Goode BL (2016). Tropomyosin and profilin cooperate to promote formin-mediated actin nucleation and drive yeast actin cable assembly. Curr Biol 26, 3230–3237.

Bashour AM, Fullerton AT, Hart MJ, Bloom GS (1997). IQGAP1, a Rac- and Cdc42-binding protein, directly binds and cross-links microfilaments. J Cell Biol 137, 1555–1566.

Bensenor LB, Kan HM, Wang N, Wallrabe H, Davidson LA, Cai Y, Schafer DA, Bloom GS (2007). IQGAP1 regulates cell motility by linking growth factor signaling to actin assembly. J Cell Sci 120, 658–669.

Brandt DT, Marion S, Griffiths G, Watanabe T, Kaibuchi K, Grosse R (2007). Dia1 and IQGAP1 interact in cell migration and phagocytic cup formation. J Cell Biol 178, 193–200.

Breitsprecher D, Jaiswal R, Bombardier JP, Gould CJ, Gelles J, Goode BL (2012). Rocket launcher mechanism of collaborative actin assembly defined by single-molecule imaging. Science 336, 1164–1168.

Casella JF, Maack DJ, Lin S (1986). Purification and initial characterization of a protein from skeletal muscle that caps the barbed ends of actin filaments. J Biol Chem 261, 10915–10921.

Dong P, Nabeshima K, Nishimura N, Kawakami T, Hachisuga T, Kawarabayashi T, Iwasaki H (2006). Overexpression and diffuse expression pattern of IQGAP1 at invasion fronts are independent prognostic parameters in ovarian carcinomas. Cancer Lett 243, 120–127.

Epp JA, Chant J (1997). An IQGAP-related protein controls actin-ring formation and cytokinesis in yeast. Curr Biol 7, 921–929.

Fukata M, Kuroda S, Fujii K, Nakamura T, Shoji I, Matsuura Y, Okawa K, Iwamatsu A, Kikuchi A, Kaibuchi K (1997). Regulation of cross-linking of actin filament by IQGAP1, a target for Cdc42. J Biol Chem 272, 29579–29583.

Fukata M, Watanabe T, Noritake J, Nakagawa M, Yamaga M, Kuroda S, Matsuura Y, Iwamatsu A, Perez F, Kaibuchi K (2002). Rac1 and Cdc42 capture microtubules through IQGAP1 and CLIP-170. Cell 109, 873–885.

Goodman A, Goode BL, Matsudaira P, Fink GR (2003). The Saccharomyces cerevisiae calponin/transgelin homolog Scp1 functions with fimbrin to regulate stability and organization of the actin cytoskeleton. Mol Biol Cell 14, 2617–2629.

Graziano BR, Yu HY, Alioto SL, Eskin JA, Ydenberg CA, Waterman DP, Garabedian M, Goode BL (2014). The F-BAR protein Hof1 tunes formin activity to sculpt actin cables during polarized growth. Mol Biol Cell 25, 1730–1743.

Grohmanova K, Schlaepfer D, Hess D, Gutierrez P, Beck M, Kroschewski R (2004). Phosphorylation of IQGAP1 modulates its binding to Cdc42, revealing a new type of rho-GTPase regulator. J Biol Chem 279, 48495–48504.

Hart MJ, Callow MG, Souza B, Polakis P (1996). IQGAP1, a calmodulin-binding protein with a rasGAP-related domain, is a potential effector for cdc42Hs. EMBO J 15, 2997–3005.

Hayakawa Y, Takain M, Imai T, Yamada MD, Hirose K, Ngo KX, Kodera N, Tokuraku K, Numata O, Nakano K, Uyeda TQP (2020). Actin binding domain of Rng2 strongly inhibits actin movement on myosin II HMM through structural changes of actin filaments. BioRxiv doi:10.1101/2020.04.14.041046.

Hedman AC, Smith JM, Sacks DB (2015). The biology of IQGAP proteins: beyond the cytoskeleton. EMBO Rep 16, 427–446.

Henty-Ridilla JL, Rankova A, Eskin JA, Kenny K, Goode BL (2016). Accelerated actin filament polymerization from microtubule plus ends. Science 352, 1004–1009.

Ho YD, Joyal JL, Li Z, Sacks DB (1999). IQGAP1 integrates Ca2+/calmodulin and Cdc42 signaling. J Biol Chem 274, 464–470.

Jadeski L, Mataraza JM, Jeong HW, Li Z, Sacks DB (2008). IQGAP1 stimulates proliferation and enhances tumorigenesis of human breast epithelial cells. J Biol Chem 283, 1008–1017.

Jegou A, Carlier MF, Romet-Lemonne G (2011a). Microfluidics pushes forward microscopy analysis of actin dynamics. Bioarchitecture 1, 271–276.

Jegou A, Niedermayer T, Orban J, Didry D, Lipowsky R, Carlier MF, Romet-Lemonne G (2011b). Individual actin filaments in a microfluidic flow reveal the mechanism of ATP hydrolysis and give insight into the properties of profilin. PLoS Biol 9, e1001161.

Johnston AB, Hilton DM, McConnell P, Johnson B, Harris MT, Simone A, Amarasinghe GK, Cooper JA, Goode BL (2018). A novel mode of capping protein-regulation by twinfilin. eLife 7, e41313.

Koestler SA, Rottner K, Lai F, Block J, Vinzenz M, Small JV (2009). F- and G-actin concentrations in lamellipodia of moving cells. PloS One 4, e4810.

Korenbaum E, Rivero F (2002). Calponin homology domains at a glance. J Cell Sci 115, 3543–3545.

Kuhn JR, Pollard TD (2005). Real-time measurements of actin filament polymerization by total internal reflection fluorescence microscopy. Biophys J 88, 1387–1402.

Kuroda S, Fukata M, Kobayashi K, Nakafuku M, Nomura N, Iwamatsu A, Kaibuchi K (1996). Identification of IQGAP as a putative target for the small GTPases, Cdc42 and Rac1. J Biol Chem 271, 23363–23367.

Le Clainche C, Schlaepfer D, Ferrari A, Klingauf M, Grohmanova K, Veligodskiy A, Didry D, Le D, Egile C, Carlier MF, Kroschewski R (2007). IQGAP1 stimulates actin assembly through the N-WASP-Arp2/3 pathway. J Biol Chem 282, 426–435.

LeCour L Jr, Boyapati VK, Liu J, Li Z, Sacks DB, Worthylake DK (2016). The structural basis for Cdc42-induced dimerization of IQGAPs. Structure 24, 1499–1508.

Lewkowicz E, Herit F, Le Clainche C, Bourdoncle P, Perez F, Niedergang F (2008). The microtubule-binding protein CLIP-170 coordinates mDia1 and actin reorganization during CR3-mediated phagocytosis. J Cell Biol 183, 1287–1298.

Liu J, Kurella VB, LeCour L Jr, Vanagunas T, Worthylake DK (2016). The IQGAP1 N-terminus forms dimers, and the dimer interface is required for binding F-actin and calcium-bound calmodulin. Biochemistry 55, 6433–6444.

Loisel TP, Boujemaa R, Pantaloni D, Carlier MF (1999). Reconstitution of actin-based motility of Listeria and Shigella using pure proteins. Nature 401, 613–616.

Mataraza JM, Briggs MW, Li Z, Entwistle A, Ridley AJ, Sacks DB (2003). IQGAP1 promotes cell motility and invasion. J Biol Chem 278, 41237–41245.

Mateer SC, McDaniel AE, Nicolas V, Habermacher GM, Lin MJ, Cromer DA, King ME, Bloom GS (2002). The mechanism for regulation of the F-actin binding activity of IQGAP1 by calcium/calmodulin. J Biol Chem 277, 12324–12333.

Okada K, Bartolini F, Deaconescu AM, Moseley JB, Dogic Z, Grigorieff N, Gundersen GG, Goode BL (2010). Adenomatous polyposis coli protein nucleates actin assembly and synergizes with the formin mDia1. J Cell Biol 189, 1087–1096.

Palani S, Ghosh S, Ivorra-Molla E, Clarke S, Suchenko A, Balasubramanian MK, Koster DV (2021). Calponin-homology domain mediated bending of membrane-associated actin filaments. eLife 10, e61078.

Pelikan-Conchaudron A, Le Clainche C, Didry D, Carlier MF (2011). The IQGAP1 protein is a calmodulin-regulated barbed end capper of actin filaments: possible implications in its function in cell migration. J Biol Chem 286, 35119–35128.

Pollard TD (1986). Rate constants for the reactions of ATP- and ADP-actin with the ends of actin filaments. J Cell Biol 103, 2747–2754.

Pollard TD, Blanchoin L, Mullins RD (2000). Molecular mechanisms controlling actin filament dynamics in nonmuscle cells. Annu Rev Biophys Biomol Struct 29, 545–576.

Ren JG, Li Z, Crimmins DL, Sacks DB (2005). Self-association of IQGAP1: characterization and functional sequelae. J Biol Chem 280, 34548–34557.

Roy M, Li Z, Sacks DB (2004). IQGAP1 binds ERK2 and modulates its activity. J Biol Chem 279, 17329–17337.

Shannon KB (2012). IQGAP family members in yeast, Dictyostelium, and mammalian cells. Int J Cell Biol 2012, 894817.

Shannon KB, Li R (1999). The multiple roles of Cyk1p in the assembly and function of the actomyosin ring in budding yeast. Mol Biol Cell 10, 283–296.

Shekhar S (2017). Microfluidics-assisted TIRF imaging to study single actin filament dynamics. Curr Protoc Cell Biol 77, 12.13.11–12.13.24.

Shekhar S, Carlier MF (2016). Single-filament kinetic studies provide novel insights into regulation of actin-based motility. Mol Biol Cell 27, 1–6.

Shekhar S, Carlier MF (2017). Enhanced depolymerization of actin filaments by ADF/cofilin and monomer funneling by capping protein cooperate to accelerate barbed-end growth. Curr Biol 27, 1990–1998.e1995.

Smith BA, Gelles J, Goode BL (2014). Single-molecule studies of actin assembly and disassembly factors. Methods Enzymol 540, 95–117.

Soeno Y, Abe H, Kimura S, Maruyama K, Obinata T (1998). Generation of functional beta-actinin (CapZ) in an E. coli expression system. J Muscle Cell Motil 19, 639–646.

Spudich JA, Watt S (1971). The regulation of rabbit skeletal muscle contraction. I. Biochemical studies of the interaction of the tropomyosin-troponin complex with actin and the proteolytic fragments of myosin. J Biol Chem 246, 4866–4871.

Sweeney MO, Collins A, Padrick SB, Goode BL (2015). A novel role for WAVE1 in controlling actin network growth rate and architecture. Mol Biol Cell 26, 495–505.

Watanabe T, Wang S, Noritake J, Sato K, Fukata M, Takefuji M, Nakagawa M, Izumi N, Akiyama T, Kaibuchi K (2004). Interaction with IQGAP1 links APC to Rac1, Cdc42, and actin filaments during cell polarization and migration. Dev Cell 7, 871–883.

Wear MA, Yamashita A, Kim K, Maeda Y, Cooper JA (2003). How capping protein binds the barbed end of the actin filament. Curr Biol 13, 1531–1537.

Weissbach L, Settleman J, Kalady MF, Snijders AJ, Murthy AE, Yan YX, Bernards A (1994). Identification of a human rasGAP-related protein containing calmodulin-binding motifs. J Biol Chem 269, 20517–20521.

White CD, Brown MD, Sacks DB (2009). IQGAPs in cancer: a family of scaffold proteins underlying tumorigenesis. FEBS Lett 583, 1817–1824.

Wu JQ, Kuhn JR, Kovar DR, Pollard TD (2003). Spatial and temporal pathway for assembly and constriction of the contractile ring in fission yeast cytokinesis. Dev Cell 5, 723–734.

Wu JQ, Pollard TD (2005). Counting cytokinesis proteins globally and locally in fission yeast. Science 310, 310–314.